

A Study of Radio Knots within Supernova Remnant Cassiopeia A

XIANHUAN LEI ^{1,2} HUI ZHU,¹ HAIYAN ZHANG,^{1,3} WENWU TIAN,^{1,2,4} AND DAN WU¹

¹*National Astronomical Observatories, Chinese Academy of Sciences, 20A Datun Road, Chaoyang District, Beijing 100012, China; zhuhui@bao.ac.cn, twu@bao.ac.cn, hyzhang@nao.cas.cn*

²*School of Astronomy and Space Science, University of Chinese Academy of Sciences, Beijing 100049, China*

³*CAS Key Laboratory of FAST, National Astronomical Observatories, Chinese Academy of Sciences, Beijing 100101, China*

⁴*The Key Laboratory of Cosmic Rays (Tibet University), Ministry of Education, Lhasa 850000, China*

ABSTRACT

The study on the dynamic evolution of young supernova remnants (SNRs) is an important way to understand the density structure of the progenitor's circumstellar medium. We have reported the acceleration or deceleration, proper motion and brightness changes of 260 compact radio features in the second youngest known SNR Cas A at 5 GHz based on the VLA data of five epochs from 1987 to 2004. The radio expansion center locates at $\alpha(1950) = 23^{\text{h}}21^{\text{m}}9^{\text{s}}7 \pm 0^{\text{s}}29$, $\delta(1950) = +58^{\circ}32'25''.2 \pm 2''.2$. Three-quarters of the compact knots are decelerating, this suggests that there are significant density fluctuations in the stellar winds of the remnant's progenitor. We have verified that the acceleration or deceleration of compact knots are not related with the distribution of brightness. The brightening, fading, disappearing or new appearing of compact radio features in Cas A suggests that the magnetic field in the remnant is changing rapidly.

Keywords: Supernova Remnant — Cassiopeia A — Proper motion

1. INTRODUCTION

Supernova remnants (SNRs) are the result of supernova (SN) ejecta interaction with the interstellar medium (ISM). The density structure of the ISM can be revealed by the early dynamic evolution of young SNRs (Inoue et al. 2012; Sano & Fukui 2021). Cassiopeia A (Cas A; 111.7-2.1), with the expansion date estimated around A.D. 1680 (Ashworth 1980; Fesen et al. 2006), is the second-youngest known Galactic SNR, at a distance of ~ 3.4 kpc (Reed et al. 1995). The observed light echoes in Cas A suggests that this remnant came from a Type IIb SN explosion (Krause et al. 2008). With the observations from the longest radio wave to very high energy γ -ray (Bell et al. 1975; Morse et al. 2004; Gotthelf et al. 2001; Ahnen et al. 2017), Cas A is one of the most-studied objects in the sky.

Multi-wavelength kinematics analysis of fragmented filaments or knots in shock provides important information about the radiative and dynamical evolution of Cas A. Generally, bright optical knots and X-ray knots of Cas A are not consistent due to the differences of temperature and density (Patnaude & Fesen 2014), the size of X-ray knots ($\sim 1.0'' - 5.0''$: Patnaude & Fesen 2007) appears to be 10 times of optical knots ($\sim 0.2'' - 0.3''$: Fesen et al. 2001). In radio bands, the shell of Cas A has two obvious features, a bright ring with a radius of ~ 1.7 pc, and a faint plateau extending to a radius of ~ 2.5 pc (Zirakashvili et al. 2014). The radio knots mainly distribute in the two regions, and cover a variety of spatial scales (Tuffs 1986).

Difference in spectroscopy and velocities has divided the optical emission in Cas A into three distinct types: 1) fast-moving knots (FMKs) with velocities from 4000 km s^{-1} to 6000 km s^{-1} (Fesen et al. 1988; Thorstensen et al. 2001), which have strong O, Si, S, Ar, Ca emission line but no H or He emission (Chevalier & Kirshner 1978, 1979); 2) quasi-stationary flocculi (QSF) with velocities less than 500 km s^{-1} (Fesen et al. 1988) and exhibit H, He, N emission (Chevalier & Kirshner 1978, 1979); 3) fast-moving flocculi (FMF), which is the outlying faint emission knots of the remnant with velocities between 6500 km s^{-1} and 8600 km s^{-1} (Fesen et al. 1987, 1988), and have H, S and N emission (Fesen 2001).

Similar to optical emission, the X-ray spectrum with O, Si, S, Ar, Ni, Ca and Fe emission lines, and the spatial distribution of element abundances in X-ray ejecta reveals the nucleosynthesis processes of SN explosion (Hughes et al. 2000; Willingale et al. 2002; DeLaney et al. 2004; Hwang & Laming 2012). Non-thermal radiation extends to hard

X-rays in both the forward and reverse shock (Allen et al. 1997; Grefenstette et al. 2015). The non-thermal faint X-ray filaments or knots located at the edge of Cas A and thus identifies the forward shock whose expansion velocity has been measured in the range of $\sim 4000 \text{ km s}^{-1}$ to 6000 km s^{-1} (Gotthelf et al. 2001; DeLaney & Rudnick 2003; Patnaude & Fesen 2009; Vink et al. 2022). Helder & Vink (2008) had shown that most of non-thermal X-ray emission comes from fragmented filaments in reverse-shock, with the reverse-shock showed obvious asymmetry (Uchiyama & Aharonian 2008). The reverse-shock ejecta has an expansion velocity of $\sim 5000 \text{ km s}^{-1}$, while the shock velocity at west reached to 6000 km s^{-1} (Patnaude & Fesen 2007; Maeda et al. 2009; Sato et al. 2018; Orlando et al. 2022).

High-resolution observations of Cas A made by aperture synthetic systems provide important approach for detection the evolution of radio emission and the detailed sampling of velocity field. Bell (1977) compared two images taken by Cambridge Telescope at 5 GHz in 1969 and 1974 (Rosenberg 1970; Bell et al. 1975), the flux changes and proper motion of 34 compact radio peaks were measured. Combined with the observations of NRAO interferometer at 8.19 GHz in 1976 and 2.7 GHz in 1967, the evolution of 83 radio emission features had been studied, of which $\sim 30\%$ were brightening (Dickel & Greisen 1979; Hogg et al. 1969). Tufts (1986) made an observation by Cambridge 5-km Telescope at 5 GHz in 1978 and compared the observation made by Bell et al. (1975) in 1974, measured proper motion and brightness changes of 342 compact radio features. There was no relationship between proper motion and brightness change. Anderson & Rudnick (1995: AR95) calculated the proper motion and brightness changes of 304 radio knots using the least-square method, which combined observations of Cambridge 5-km Telescope and Very Large Array (VLA¹) at 5 GHz for 6 epochs (Cambridge 5-km Telescope: 1978, 1982; VLA: 1983, 1985, 1987, 1990). The radio emission plasma in Cas A was decelerating significantly, and the bulk expansion age was 2.5–4 times the actual age of the remnant. Brighter knots appear to be steeper spectra, and do not find the correlation between spectral index and brightness changes (Anderson & Rudnick 1996).

In this work, we report the progenitor’s circumstellar medium density distribution of Cas A by studying the motion and brightness changes of the radio emissions in the remnant. We use the VLA archival visibility observation data for Cas A at 5 GHz including five epochs of 1987, 1994, 1997, 2000 and 2004. These data were observed in the A-, B-, C- and D-configuration of VLA, which has a high-sensitivity and high-resolution of $1.5''$. For this paper, Section 2 describes the data used and the data calibration process, Section 3 is the calculation for the proper motion and brightness changes of compact radio peaks, the results and discussion are shown in the Section 4.

2. DATA SAMPLE AND CALIBRATION

The data used in this study is the VLA archival² C-band (5 GHz; $\lambda=6 \text{ cm}$) standard-configuration data of Cas A. Each data was obtained at several frequencies around the nominal observing frequency of 5 GHz, which improves the aperture coverage. In the VLA standard-configurations, the A-configuration is the most diffuse, with a maximum baseline of 36.4 km and a resolution of 0.33 arcsec in C-Band; D-configuration is the most compact, with the shortest baseline of 0.035 km. The details of the data we used are summarized in Table 1, which covers 5 epochs of 1987.73 (Project: AB0434), 1994.75 (Project: AR0310), 1997.67 (Project: AR0378), 2000.82 (Project: AR0435) and 2004.74 (Project: AD0500), with total time baseline spanning about 17 yrs. In order to sample the complex spatial structure of Cas A, the aperture coverage has been maximized.

These data calibration procedure has performed by the Common Astronomy Software Applications package (CASA³: McMullin et al. 2007). The calibrations of the primary flux density in all observing sessions are based on the 0134+329 (3C48), and the 2352+4995 is the phase calibrators. The antenna position was first calibrated, then we determined the flux density scale, complex gain, and baseline-based solutions from the calibrator 3C48, and applied them to the target Cas A (3C461). Data for each array were calibrated individually, and then concatenated and imaged. To avoid negative "bowl" around the source, Multi-Scale Clean deconvolution method was used for imaging (Cornwell 2008). We have used briggs weighting with different parameters of robust=-2, -1, 0, 1, 2 to restore images. When robust=1 and 2, images are in high random noise of VLA, and rms noise reaches 30 mJy beam^{-1} . In the absolute flux scale uncertainty of 3% (Perley & Butler 2013), there are same integrated flux density and stable noise levels for robust=-2,

¹ <https://science.nrao.edu/facilities/vla>

² <https://archive.nrao.edu/archive/archiveproject.jsp>

³ <https://casa.nrao.edu/>

Table 1. Summary of VLA observation for Cas A from 1987 to 2005, $\lambda = 6$ cm.

Date	VLA	Frequencies	Bandwidth	On-Source Time	Observer
year	configuration	GHz	MHz	minutes	
AB0434(1987–1988)					
1987.58	A	4.64, 4.97	3.125	420	L.Rudnick
1987.62	A	4.41, 5.08	3.125	325	L.Rudnick
1987.77	A	4.97, 4.64, 4.41, 5.08	3.125	330	L.Rudnick
1987.88	B	4.97, 4.64	6.25	357	L.Rudnick
1988.19	C, D	4.87, 4.82	12.5	53	L.Rudnick
1987.35	D	4.89, 4.84	50	30	L.Rudnick
AR0310(1994–1995)					
1994.23	A	4.41, 4.64, 4.97, 5.08, 4.97	3.125	545	L.Rudnick
1994.58	B	4.41, 4.99, 4.64, 5.09	12.5	283	L.Rudnick
1994.96	C	4.41, 4.99, 4.64, 5.09	12.5	182	L.Rudnick
1995.23	D	4.41, 4.99, 4.64, 5.08	12.5	108	L.Rudnick
AR0378(1997–1998)					
1998.22	A	4.41, 4.99, 4.64, 5.08	6.25	453	L.Rudnick
1997.38	B	4.41, 4.99, 4.64, 5.08	12.5	304	L.Rudnick & B.Koralesky
1997.70	C	4.41, 4.99, 4.64, 5.08	12.5	142	L.Rudnick & B.Koralesky
1997.36	D	4.41, 4.99, 4.64, 5.08	12.5	123	L.Rudnick
AR0435(2000–2001)					
2000.94	A	4.72, 5.0, 4.86, 4.61	6.25	537	L.Rudnick
2001.33	B	4.72, 4.99, 4.86, 4.6	12.5	468	L.Rudnick
2000.31	C	4.72, 5.0, 4.6, 4.86	25	241	L.Rudnick
2000.68	D	4.72, 5.0, 4.86, 4.6	12.5	183	L.Rudnick
AD0500(2004–2005)					
2004.73	A	4.72, 4.99, 4.86, 4.61	6.25	481	T.Delaney
2005.35	B	4.86, 4.61, 4.72, 5.0	12.5	334	T.Delaney
2004.24	C	4.72, 5.0, 4.86, 4.6	25	225	T.Delaney
2004.62	D	4.71, 4.99, 4.86, 4.61	50	163	T.Delaney

-1 and 0. Considering surface brightness sensitivity while requiring high-resolution, we used robust=0 for the images restore, obtained images with a rms noise of $3.0 \text{ mJy beam}^{-1}$.

3. METHOD

AR95 has performed a detailed study for the temporal evolution of compact radio features in Cas A. The net radial deceleration of compact radio features in Cas A has not been observed. In this section, we have made a new measurement of the proper motion and brightness changes for the radio features based on the higher resolution ($1.5''$) and sensitivity observations of VLA.

3.1. Image Normalization

The five images have been obtained from difference observation projects over five epochs. These observations exist differences in absolute flux calibration and aperture coverage, which leads to the differences of these five images' reconstruction. In order to minimize the effect of different aperture coverage for imaging, image normalization is necessary. In the five images, AR310 (1994.75 epoch) has the highest resolution ($0.56'' \times 0.46''$) and AD500 (2004.74 epoch) has the lowest resolution ($1.42'' \times 1.2''$). To compare the flux density of different observations safely, we adopt the gaussian convolution algorithm to smooth all images into the same beamsize of $1.5''$.

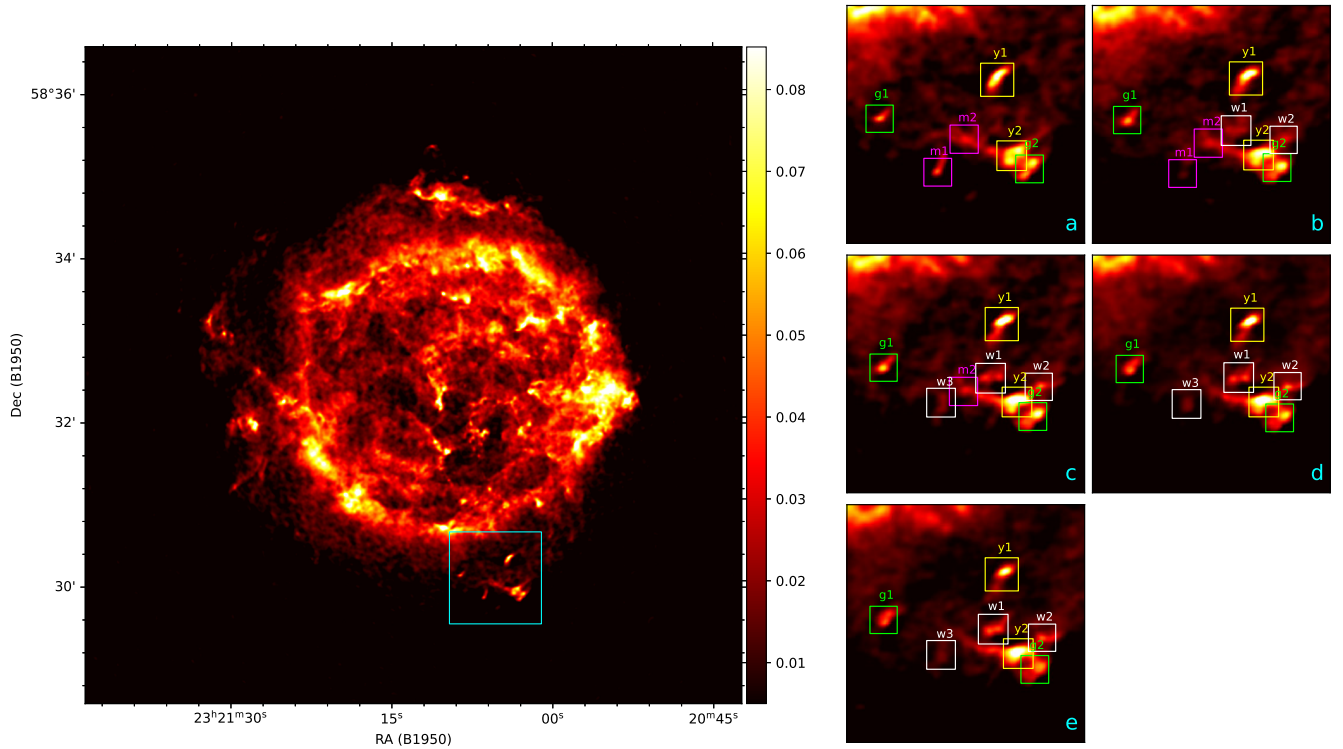


Figure 1. The continuum images of Cas A at $\lambda = 6$ cm, Color-scale is in units of Jy beam^{-1} . Left panel: the image of 1987, which combines the A, B, C and D-configuration of VLA. Right panel: the local evolution of Cas A from 1987 to 2004 (the cyan box region on the left panel). Local images of a, b, c, d and e are the 1987 (Project: AB0434), 1994 (Project: AR0310), 1997 (Project: AR0378), 2000 (Project: AR0435) and 2004 (Project: AD0500), respectively. Using the earliest observed image of 1987 as the reference image, the knots in yellow boxes indicates that the knots currently brightening, examples y1 (knot 7) and y2 (knot 5) are brightening from 1987 to 2004. Knots in the green boxes indicates the knots is fading, g1 (knot 3) and g2 (knot 6) are fading from 1987 to 2004. A knot in magenta box will disappear, such as m1 evolves to 1997 and m2 to 2000. In the white boxes shows newly knots, like w1 and w2 appearing in 1994 and w3 appearing in 1997.

3.2. Selection of Compact Radio Emission Features

Hundreds of compact radio emission features in the remnant of Cas A are evolving rapidly, and parts of the knots are disappearing. To select the radio knots, we denote the location of all local maximum values based on the 1987 image, and construct the contour map. Therefore, we obtain all possible knots in the 1987 image. These knots evolve rapidly, as shown in Figure 1. In this study, we keep the knots having the following features: it can be isolated from the surroundings; clearly visible in the five continuous images of C-Band; its shape has not changed significantly over the span of 17 yrs. As a result, 260 radio knots have been kept, parts of them are consistent with the 304 knots compiled in AR95. The position of these knots are shows in Figure 2, and the detailed statistics are given in Table 2.

3.3. Measurement of Position and Brightness Relative Change

For the position and brightness change of compact features, the least-squares method is widely used (Tuffs 1986; Anderson & Rudnick 1995). This numerical method allows us to test acceleration or deceleration of individual knots, which can minimize the effect of different apertures coverage at multi-epochs on the variations of large-scale background reconstruction. We have adopted the same algorithm to measure the positions and brightness changes of each radio knot from epoch 1987 to 2004.

First, we use the epoch 1987 image(the earliest image we used, and have a high resolution) as the reference image A_{ij} , the other as comparison images B_{ij} (images from epochs 1994, 1997, 2000 and 2004). A small region is set around each knot of the reference image A_{ij} . Next, we select a region for each corresponding knots in comparison images B_{ij} , which would contain knot for all epochs and is separated from the surrounding emission. Finally, we minimize the

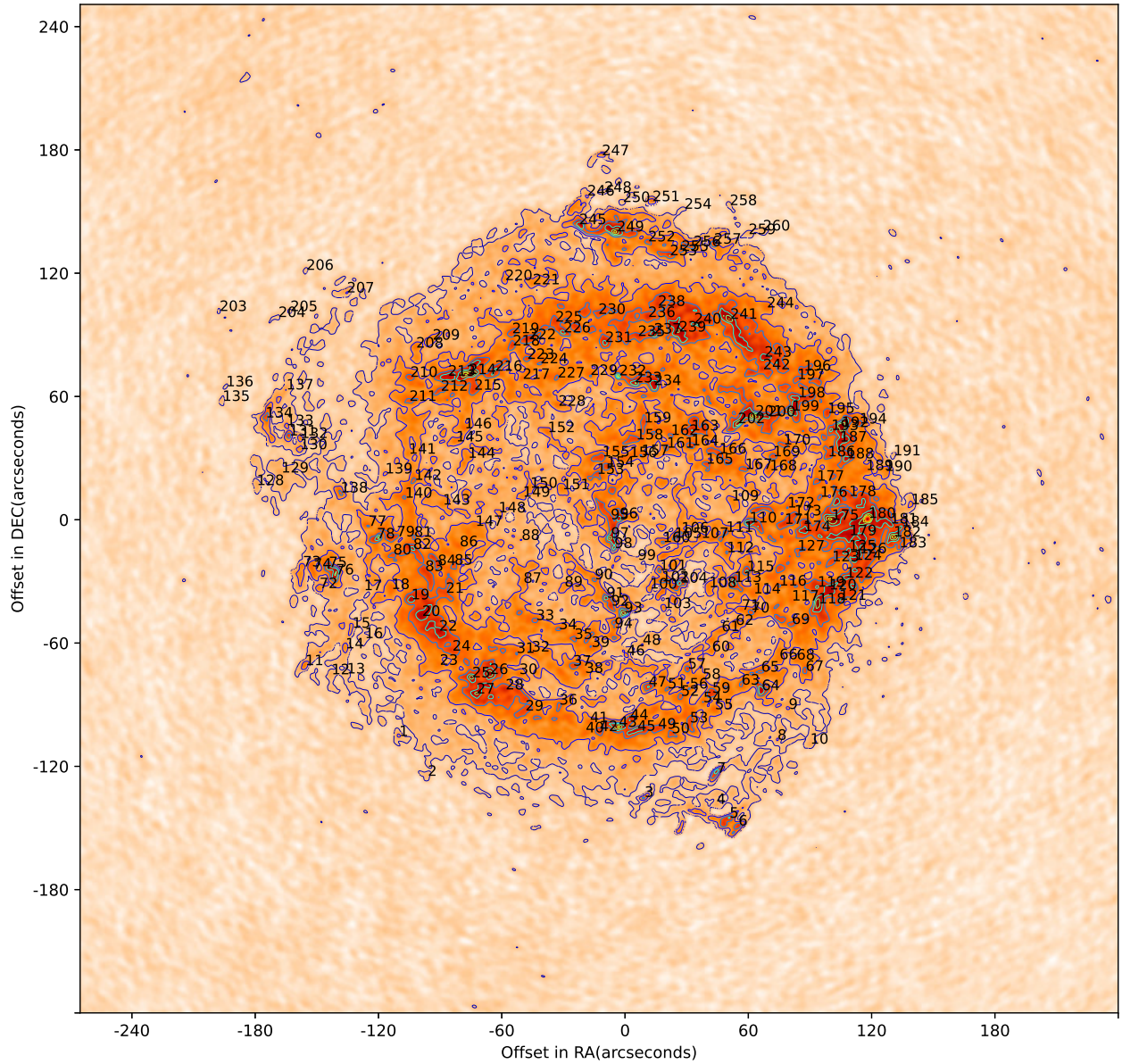


Figure 2. Position of the compact radio knots in Cas A constructed from the 1987 5 GHz observations. Contour levels in Jy beam^{-1} are 0, 0.002, 0.004, 0.006, 0.008, 0.010, 0.025, 0.05, 0.075, 0.1, 0.12, 0.14, 0.15, 0.16, 0.18, 0.19 and 0.20.

quantity in the region by the following method:

$$T(\xi) = \sum_{i=1}^I \sum_{j=1}^J Q_{ij}^2(\xi), \quad (1)$$

the summation $T(\xi)$ is performed over all pixels in the region ($I \times J$). Where, $Q_{ij}(\xi) = A_{ij} - SB_{ij}(\Delta\alpha, \Delta\sigma) - H$, with respect to 4-vector $\xi = (\Delta\alpha, \Delta\sigma, S, H)$. S is the brightness scaling factor between different epochs, $\Delta\alpha$ and $\Delta\sigma$ are the variations of the relative position between image A_{ij} and B_{ij} , H is the level of change in the local backgrounds. This summation procedure was performed four times at each radio knots to obtain the relative changes of position and brightness in four comparison images and reference image.

Table 2. Summary of VLA observations for Cas A from 1987 to 2005, $\lambda = 6$ cm.

knots (1)	knot _{A95} (2)	x (3)	y (4)	Box _{x1} (5)	Box _{x2} (6)	Box _{y1} (7)	Box _{y2} (8)	v_x (9)	δv_x (10)	v_y (11)	δv_y (12)	a_x (13)	δa_x (14)	a_y (15)	δa_y (16)	Peak Brightness (17)	$\frac{\Delta B}{B}$ (18)	$\delta \frac{\Delta B}{B}$ (19)
1	22	-97.1	-109.7	-103.1	-115.9	-92.0	-105.4	-0.069	0.04	-0.177	0.01	0.0014	0.0012	0.0026	0.0031	28.53	0.087	0.034
2	2	-83.2	-129.0	-88.0	-134.9	-78.8	-124.7	-0.092	0.006	-0.221	0.04	-0.0001	0.0013	0.0021	0.0021	17.13	0.177	0.031
3	6	22.3	-139.3	16.7	-146.4	28.5	-135.1	0.019	0.016	-0.101	0.009	0.0014	0.0014	0.0002	0.0018	54.54	0.068	0.017
4	...	57.3	-142.7	54.5	-147.7	60.3	-139.9	-0.042	0.019	-0.005	0.022	0.0013	0.0014	-0.0038	0.0012	21.2	0.13	0.018
5	11	63.7	-149.4	59.1	-155.5	68.0	-146.5	-0.264	0.072	-0.103	0.006	0.0128	0.0025	0.0006	0.0014	77.13	0.069	0.01
6	13	68.0	-153.2	64.1	-158.6	74.4	-150.4	0.126	0.016	-0.173	0.016	-0.0008	0.0026	0.0022	0.003	69.28	0.036	0.01
7	9	57.5	-127.5	50.8	-133.8	65.5	-121.3	0.137	0.024	0.042	0.014	-0.0028	0.0016	-0.0026	0.0009	87.47	0.039	0.011
8	73	87.0	-111.5	84.1	-116.0	94.6	-105.9	0.312	0.051	0.001	0.021	-0.0132	0.003	-0.0037	0.0016	27.13	0.078	0.034
9	76	92.4	-96.4	88.8	-106.0	101.0	-93.6	0.299	0.152	-0.538	0.188	-0.0227	0.0066	0.0329	0.0124	26.78	0.018	0.05
10	79	103.0	-113.4	99.3	-120.9	111.7	-109.3	0.18	0.03	-0.282	0.074	-0.0007	0.004	0.0137	0.0028	22.73	0.019	0.017
11	15	-142.8	-75.2	-150.2	-82.8	-139.7	-72.0	-0.265	0.015	-0.295	0.019	0.0008	0.0037	0.0047	0.0029	43.44	-0.063	0.009
12	16	-130.0	-79.6	-136.0	-85.8	-127.5	-76.8	-0.03	0.039	-0.248	0.07	-0.0063	0.0036	0.0088	0.0029	21.03	-0.03	0.008
13	17	-122.6	-79.2	-127.7	-85.7	-119.0	-76.5	-0.256	0.073	-0.065	0.091	0.0061	0.0021	-0.0042	0.0038	84.62	0.368	0.098
14	...	-123.2	-67.0	-129.1	-75.1	-119.8	-63.6	-0.12	0.029	-0.363	0.047	-0.001	0.0035	-0.0099	0.004	34.55	-0.028	0.012
15	18	-119.9	-57.0	-125.6	-64.8	-116.3	-51.8	-0.109	0.014	-0.264	0.027	-0.0018	0.0021	0.0041	0.0026	28.64	0.063	0.038
16	19	-113.8	-62.0	-118.1	-66.5	-107.0	-57.5	-0.056	0.134	-0.033	0.034	0.0015	0.0046	-0.0041	0.0085	16.64	0.075	0.026
17	96	-114.3	-38.7	-120.0	-45.3	-112.1	-35.6	-0.177	0.037	-0.124	0.092	0.004	0.0079	0.0075	0.01	35.56	-0.027	0.011
18	21	-100.9	-38.1	-109.5	-45.3	-97.1	-34.2	-0.165	0.007	-0.153	0.036	-0.0014	0.0026	0.0088	0.0019	45.71	0.008	0.009
19	23	-91.2	-43.1	-95.7	-47.7	-86.4	-38.6	-0.163	0.02	-0.083	0.013	0.004	0.0014	0.0015	0.0008	87.34	-0.02	0.006
20	25	-86.0	-51.2	-91.3	-56.4	-81.6	-46.0	-0.129	0.044	-0.054	0.015	0.0038	0.0058	0.0002	0.0017	98.97	-0.03	0.001
21	27	-74.4	-40.0	-78.8	-44.1	-70.9	-36.7	-0.037	0.011	-0.08	0.011	0.0005	0.0016	0.0012	0.0009	60.87	0.122	0.04
22	26	-77.7	-58.4	-82.1	-63.2	-73.9	-55.3	-0.044	0.006	-0.095	0.019	-0.0015	0.0011	0.0047	0.0015	93.16	-0.013	0.009
23	...	-77.4	-75.0	-82.2	-80.2	-73.6	-71.3	0.002	0.021	-0.08	0.032	-0.0005	0.0023	-0.0015	0.0038	42.62	0.04	0.02
24	...	-71.2	-68.1	-78.5	-73.6	-66.9	-64.0	-0.063	0.089	-0.178	0.046	-0.0069	0.0065	0.0086	0.0017	65.59	0.022	0.018
25	28	-61.6	-81.1	-68.2	-86.4	-58.1	-77.1	-0.139	0.018	-0.088	0.005	-0.0025	0.003	0.0003	0.0012	115.81	-0.016	0.006
26	30	-52.9	-79.5	-58.1	-84.8	-46.4	-73.8	-0.182	0.112	-0.237	0.133	0.0181	0.0074	0.0205	0.0103	114.94	-0.022	0.004
27	...	-59.5	-88.9	-64.0	-93.0	-54.3	-83.4	-0.057	0.021	0.026	0.017	0.0028	0.001	0.0001	0.0012	104.83	0.006	0.005
28	...	-45.3	-87.0	-52.4	-92.6	-42.0	-84.0	-0.243	0.035	-0.067	0.023	0.0064	0.0025	-0.0044	0.0023	74.81	0.028	0.013
29	33	-35.7	-97.3	-40.2	-102.0	-30.5	-92.8	0.02	0.01	-0.02	0.017	-0.0012	0.0002	-0.002	0.0016	61.92	0.001	0.005
30	...	-38.7	-79.5	-43.1	-83.8	-34.5	-76.3	-0.028	0.042	0.015	0.019	-0.0015	0.004	-0.0028	0.0018	45.42	-0.024	0.006
31	32	-40.0	-69.2	-45.2	-73.3	-35.9	-65.2	0.189	0.063	-0.037	0.015	-0.0153	0.0031	0.0018	0.0021	50.82	0.06	0.024
32	34	-32.6	-68.5	-37.7	-73.5	-28.7	-64.9	-0.109	0.035	-0.028	0.022	0.0071	0.0015	-0.0036	0.002	50.8	0.097	0.032
33	...	-30.5	-53.2	-33.6	-60.7	-22.6	-50.2	0.333	0.159	-0.26	0.054	-0.0118	0.0049	0.0088	0.004	55.46	-0.047	0.016
34	35	-19.4	-57.6	-23.2	-61.1	-15.0	-54.1	0.066	0.028	0.057	0.021	-0.0019	0.0006	-0.0028	0.001	57.48	0.034	0.016

Table 2 continued on next page

Table 2 (continued)

knots	knot _{A95}	x	y	Box _{x1}	Box _{x2}	Box _{y1}	Box _{y2}	v_x	δv_x	v_y	δv_y	a_x	δa_x	a_y	δa_y	Peak Brightness	$\frac{\Delta F}{F}$	$\delta \frac{\Delta F}{F}$
(1)	(2)	(3)	(4)	(5)	(6)	(7)	(8)	(9)	(10)	(11)	(12)	(13)	(14)	(15)	(16)	(17)	(18)	(19)
35	38	-11.9	-62.4	-14.9	-64.9	-8.3	-58.5	0.018	0.016	0.052	0.032	-0.0005	0.0033	-0.0061	0.0027	57.69	-0.011	0.006
36	...	-19.2	-94.3	-23.3	-99.8	-15.6	-91.4	-0.066	0.017	0.026	0.061	0.0033	0.0018	-0.0079	0.0044	54.91	0.081	0.044
37	37	-12.5	-75.4	-16.2	-79.2	-6.6	-71.2	0.054	0.067	-0.038	0.005	0.0015	0.0029	0.0003	0.001	60.91	-0.017	0.007
38	...	-6.6	-78.9	-9.2	-81.5	-1.6	-73.6	0.21	0.043	0.201	0.028	-0.0084	0.0018	-0.0057	0.0014	45.32	0.059	0.015
39	41	-3.5	-66.3	-6.3	-71.4	3.5	-62.6	0.224	0.023	-0.022	0.013	-0.0051	0.0034	0.0003	0.0016	50.92	0.047	0.03
40	39	-6.3	-107.9	-11.3	-115.0	-3.2	-104.8	-0.103	0.039	-0.075	0.028	0.004	0.0048	-0.0073	0.0057	47.58	0.035	0.024
41	...	-4.3	-102.9	-7.7	-108.3	0.2	-100.3	0.038	0.025	-0.066	0.014	-0.0017	0.0009	-0.0025	0.0017	48.91	0.065	0.027
42	42	0.5	-107.3	-2.4	-113.3	5.0	-104.3	-0.013	0.02	-0.154	0.017	0.0013	0.0012	-0.0022	0.0029	63.99	0.028	0.014
43	44	9.8	-105.1	5.9	-110.6	15.0	-101.8	-0.016	0.016	-0.159	0.008	0.0028	0.0013	-0.0001	0.0022	122.85	0.005	0.009
44	47	15.4	-101.6	11.4	-107.4	18.9	-98.8	-0.03	0.017	-0.124	0.007	0.0007	0.0019	-0.0016	0.0021	75.3	-0.008	0.005
45	...	18.8	-107.1	11.9	-114.5	27.5	-102.8	0.039	0.011	-0.156	0.006	0.0003	0.0014	0.0015	0.0016	86.25	-0.004	0.005
46	46	13.6	-70.4	11.5	-74.0	17.7	-67.9	0.023	0.014	-0.023	0.011	0.0018	0.002	-0.0005	0.0014	39.57	-0.035	0.008
47	49	24.2	-85.6	18.3	-92.4	29.6	-81.3	-0.032	0.012	-0.174	0.02	0.0031	0.0012	0.0046	0.0015	76.47	0.038	0.008
48	48	21.4	-65.2	18.5	-69.9	25.4	-61.6	0.142	0.06	-0.18	0.045	-0.0078	0.0018	0.0068	0.0062	25.86	0.058	0.054
49	51	28.9	-106.0	25.8	-108.8	33.3	-101.8	0.067	0.042	0.117	0.06	0.0027	0.0028	-0.0046	0.0019	64.2	0.059	0.022
50	57	35.5	-108.2	33.1	-113.2	41.1	-105.9	-0.06	0.083	0.092	0.082	0.0085	0.0084	-0.0145	0.0058	62.34	0.014	0.02
51	55	33.6	-86.5	30.4	-90.8	37.9	-83.3	0.098	0.016	0.041	0.024	-0.003	0.0006	-0.0058	0.0016	57.82	0.063	0.023
52	...	40.0	-90.1	33.6	-98.3	45.9	-87.1	0.088	0.068	-0.103	0.033	-0.002	0.0148	-0.0071	0.0064	56.77	0.03	0.012
53	60	44.4	-103.0	41.2	-111.7	52.0	-98.6	0.133	0.084	-0.338	0.029	-0.0017	0.0015	0.0074	0.0028	62.27	0.083	0.018
54	...	50.9	-93.2	48.6	-97.9	56.4	-90.6	0.092	0.02	-0.137	0.02	0.0027	0.0021	0.0041	0.0011	50.42	0.079	0.027
55	64	56.6	-96.6	54.4	-102.2	62.4	-94.5	0.194	0.037	-0.06	0.074	-0.0027	0.0033	-0.0073	0.0048	49.63	-0.046	0.011
56	61	44.3	-86.5	40.6	-90.4	48.3	-83.5	0.007	0.008	-0.152	0.045	-0.0012	0.0007	0.0091	0.0017	51.46	0.041	0.023
57	59	43.4	-76.8	37.7	-81.5	47.7	-72.4	-0.046	0.03	-0.073	0.031	0.0068	0.0017	0.0031	0.0011	72.87	-0.046	0.007
58	...	50.5	-81.9	45.1	-85.8	53.4	-78.5	-0.161	0.137	-0.181	0.052	0.0054	0.0044	0.0135	0.0042	44.86	-0.01	0.009
59	63	55.3	-88.6	51.7	-93.1	60.8	-84.7	0.071	0.02	0.063	0.034	0.0083	0.0051	-0.0041	0.0056	67.08	0.035	0.019
60	...	55.1	-68.4	52.6	-75.4	59.9	-65.7	0.13	0.03	-0.173	0.123	-0.003	0.0031	-0.0054	0.0076	41.8	-0.004	0.008
61	66	59.8	-58.7	55.0	-63.0	64.3	-55.2	-0.077	0.053	-0.034	0.021	0.0001	0.004	-0.0008	0.0009	44.65	0.004	0.01
62	...	66.6	-55.5	63.7	-61.5	74.1	-52.4	0.138	0.052	-0.177	0.066	0.002	0.0024	0.0047	0.0029	43.11	-0.035	0.016
63	69	69.5	-84.6	66.7	-91.0	75.4	-81.1	0.12	0.004	-0.085	0.012	-0.0001	0.0016	-0.0026	0.0018	53.77	-0.029	0.002
64	71	79.3	-87.4	75.5	-92.5	85.6	-83.1	0.115	0.01	0.0	0.0	-0.0013	0.0012	0.0	0.0	94.41	-0.015	0.003
65	72	79.0	-78.3	76.6	-82.5	84.7	-74.2	0.167	0.038	-0.101	0.017	-0.0022	0.004	0.0034	0.0025	53.71	0.009	0.021
66	...	88.0	-72.3	84.7	-76.6	92.8	-67.4	0.137	0.024	0.054	0.015	-0.0028	0.0016	-0.0002	0.0016	41.71	0.037	0.017
67	78	100.7	-77.9	96.4	-84.8	106.3	-72.2	0.073	0.006	-0.038	0.016	0.0013	0.0013	-0.0014	0.0014	61.7	0.049	0.012
68	...	96.3	-72.4	93.1	-76.7	102.1	-68.9	0.142	0.105	0.06	0.048	-0.0018	0.0061	-0.0047	0.005	45.51	0.007	0.014
69	77	93.9	-55.1	91.2	-59.7	100.8	-52.6	0.161	0.019	-0.08	0.004	0.0023	0.0026	-0.0001	0.0011	62.22	0.013	0.011
70	70	74.3	-49.5	71.4	-53.3	79.2	-45.8	0.197	0.054	-0.013	0.009	-0.0072	0.0025	0.0	0.0006	57.15	0.014	0.012

Table 2 continued on next page

Table 2 (continued)

knots	knot _{A95}	x	y	Box _{x1}	Box _{x2}	Box _{y1}	Box _{y2}	v_x	δv_x	v_y	δv_y	a_x	δa_x	a_y	δa_y	Peak Brightness	$\frac{\Delta F}{F}$	$\delta \frac{\Delta F}{F}$
(1)	(2)	(3)	(4)	(5)	(6)	(7)	(8)	(9)	(10)	(11)	(12)	(13)	(14)	(15)	(16)	(17)	(18)	(19)
71	68	69.5	-48.2	66.4	-50.2	73.8	-45.2	0.038	0.058	-0.038	0.02	-0.0048	0.0026	0.0048	0.0026	48.96	-0.034	0.004
72	92	-135.9	-37.7	-143.2	-46.9	-133.3	-35.4	-0.255	0.014	-0.296	0.026	0.0026	0.0027	0.0039	0.0031	48.23	-0.015	0.022
73	89	-144.0	-27.1	-152.7	-34.2	-141.8	-24.1	-0.359	0.029	-0.142	0.019	0.0076	0.0036	-0.0022	0.0025	41.52	-0.056	0.007
74	90	-138.9	-28.2	-146.4	-34.8	-136.0	-20.6	-0.217	0.018	-0.021	0.019	-0.0004	0.0031	-0.0023	0.0009	48.23	0.024	0.011
75	93	-131.4	-27.4	-138.6	-31.1	-129.3	-22.4	-0.22	0.011	0.058	0.021	0.0012	0.0026	0.0002	0.0014	88.35	-0.041	0.009
76	...	-128.0	-31.0	-135.4	-36.1	-124.6	-26.7	-0.181	0.005	-0.032	0.009	0.0002	0.0024	-0.0015	0.0011	102.04	0.004	0.01
77	98	-112.1	-7.4	-117.4	-10.3	-108.6	-4.4	0.005	0.039	0.0	0.0	-0.005	0.002	0.0	0.0	51.65	-0.006	0.01
78	100	-108.0	-13.5	-115.1	-18.7	-104.3	-9.2	-0.153	0.02	-0.029	0.01	0.0012	0.0021	0.0015	0.0011	106.55	-0.033	0.005
79	103	-98.3	-12.5	-104.8	-16.0	-96.2	-8.7	-0.184	0.006	-0.01	0.016	-0.0015	0.0028	0.0028	0.001	66.76	0.001	0.008
80	102	-100.0	-21.3	-105.8	-25.1	-96.6	-16.6	-0.073	0.054	0.085	0.045	0.003	0.0009	0.0029	0.0053	60.12	-0.001	0.013
81	...	-89.8	-12.7	-96.0	-16.2	-86.9	-7.9	-0.025	0.023	0.124	0.037	-0.0075	0.0033	-0.0075	0.0029	53.77	-0.018	0.006
82	106	-90.3	-18.6	-96.7	-23.1	-86.7	-14.3	-0.174	0.02	-0.172	0.031	0.0046	0.0015	0.0042	0.0018	82.15	0.016	0.013
83	...	-84.5	-29.3	-91.0	-36.4	-79.3	-23.3	-0.035	0.026	-0.082	0.024	-0.0029	0.0018	0.0047	0.0012	67.04	0.045	0.018
84	...	-78.4	-26.5	-85.3	-31.8	-75.1	-21.1	-0.047	0.027	-0.079	0.015	-0.0043	0.0023	-0.0014	0.0016	68.99	0.007	0.004
85	111	-70.2	-26.3	-73.9	-31.5	-64.9	-22.5	0.075	0.041	-0.117	0.055	-0.0015	0.005	0.0097	0.0055	57.11	-0.015	0.017
86	113	-67.7	-17.3	-71.2	-23.6	-61.7	-14.0	0.139	0.014	-0.127	0.01	-0.0032	0.0015	0.0	0.0017	49.0	-0.023	0.009
87	...	-36.6	-35.1	-39.5	-38.4	-29.7	-24.4	0.139	0.013	0.544	0.132	0.0013	0.0022	-0.0158	0.0065	37.69	0.049	0.033
88	118	-37.5	-14.2	-42.4	-18.4	-33.6	-9.3	0.196	0.093	0.045	0.025	-0.0116	0.0077	-0.0011	0.0082	25.4	-0.016	0.052
89	124	-16.6	-36.9	-21.6	-42.4	-12.4	-33.3	-0.158	0.038	-0.015	0.02	0.0117	0.0054	-0.001	0.0015	34.51	0.109	0.036
90	126	-1.9	-33.3	-5.5	-38.7	6.5	-28.9	0.28	0.04	-0.144	0.055	-0.0012	0.0072	0.006	0.0047	54.92	-0.008	0.021
91	43	3.7	-42.3	-0.9	-45.7	7.0	-37.2	0.042	0.044	0.068	0.041	-0.0062	0.0053	0.002	0.0069	89.46	-0.024	0.007
92	...	6.1	-46.2	3.6	-51.0	10.3	-42.7	0.079	0.015	-0.074	0.015	0.0014	0.0016	0.0025	0.001	71.07	0.089	0.028
93	45	12.4	-49.5	7.3	-54.5	17.3	-44.9	0.109	0.068	-0.009	0.027	-0.0071	0.0015	-0.0042	0.0032	108.38	-0.034	0.002
94	...	7.7	-57.0	5.1	-59.5	12.2	-54.9	0.125	0.026	-0.162	0.024	-0.0041	0.0014	0.0059	0.0015	50.29	0.123	0.023
95	133	5.8	-4.2	2.2	-6.2	7.7	-0.5	-0.051	0.007	-0.018	0.028	-0.0003	0.0011	0.0063	0.0026	69.23	-0.001	0.016
96	136	10.2	-3.6	7.5	-7.5	14.7	-0.1	0.051	0.013	-0.051	0.018	0.0016	0.0018	0.0042	0.0013	92.87	-0.034	0.004
97	132	6.0	-13.2	2.3	-17.1	11.4	-8.3	0.076	0.011	0.065	0.026	-0.0003	0.0008	-0.0053	0.0014	107.81	0.078	0.024
98	135	7.6	-18.1	5.9	-22.1	12.4	-16.1	0.101	0.009	-0.044	0.006	0.0011	0.0017	-0.0015	0.0011	84.62	-0.005	0.007
99	139	19.0	-23.9	16.1	-28.7	23.5	-21.2	0.208	0.033	-0.134	0.014	-0.0055	0.0033	0.0025	0.0013	21.75	0.178	0.063
100	...	24.9	-37.9	22.4	-41.2	29.4	-34.7	0.146	0.018	0.016	0.036	-0.0044	0.0011	-0.0017	0.0034	36.36	0.094	0.01
101	141	29.6	-28.9	25.7	-32.5	33.1	-25.3	-0.064	0.012	0.026	0.017	0.0029	0.001	0.0001	0.0012	57.99	0.16	0.015
102	...	30.7	-34.4	28.3	-40.1	36.7	-32.0	0.087	0.031	-0.15	0.024	-0.0009	0.001	-0.0019	0.0031	53.3	0.114	0.049
103	54	31.8	-47.4	28.9	-50.7	35.5	-43.5	0.169	0.043	-0.112	0.034	-0.0097	0.0034	0.0087	0.0022	37.53	0.156	0.033
104	150	39.7	-35.0	37.5	-38.6	45.6	-31.5	0.172	0.031	-0.012	0.018	-0.0042	0.0018	-0.0026	0.0011	86.14	-0.053	0.013
105	...	37.0	-13.2	32.3	-23.1	40.5	-10.5	-0.207	0.06	-0.301	0.085	0.0101	0.0024	-0.0117	0.0103	57.69	0.128	0.042

Table 2 continued on next page

Table 2 (continued)

knots	knot _{A95}	x	y	Box _{x1}	Box _{x2}	Box _{y1}	Box _{y2}	v_x	δv_x	v_y	δv_y	a_x	δa_x	a_y	δa_y	Peak Brightness	$\frac{\Delta B}{B}$	$\delta \frac{\Delta B}{B}$
(1)	(2)	(3)	(4)	(5)	(6)	(7)	(8)	(9)	(10)	(11)	(12)	(13)	(14)	(15)	(16)	(17)	(18)	(19)
106	...	40.3	-10.6	37.9	-16.0	47.7	-8.0	0.007	0.102	-0.129	0.025	0.0174	0.0086	0.005	0.0035	54.56	-0.035	0.008
107	153	49.9	-13.2	46.7	-17.0	54.3	-9.8	0.083	0.013	-0.035	0.013	-0.0015	0.0007	0.0027	0.0007	49.95	0.009	0.009
108	154	53.7	-37.3	50.1	-42.3	60.1	-31.2	0.076	0.012	0.035	0.007	0.0029	0.0021	-0.0014	0.0003	41.27	0.046	0.024
109	161	64.7	5.0	61.5	-3.5	72.4	8.4	0.139	0.013	-0.287	0.091	0.0013	0.0022	0.0067	0.009	37.21	0.09	0.037
110	164	73.4	-5.7	69.0	-9.3	78.0	-1.3	-0.065	0.033	0.083	0.012	0.0035	0.003	-0.004	0.001	98.54	0.049	0.019
111	158	62.0	-10.3	59.6	-14.9	67.0	-7.7	0.196	0.056	-0.163	0.02	-0.0067	0.0014	0.004	0.0014	62.76	0.049	0.012
112	159	62.4	-20.2	59.3	-24.7	67.3	-16.4	0.146	0.018	0.001	0.02	-0.0044	0.0011	-0.0024	0.0019	52.0	0.035	0.014
113	160	66.0	-34.7	61.9	-40.7	71.9	-27.2	0.029	0.012	0.009	0.04	0.003	0.0015	0.0085	0.003	85.29	-0.038	0.01
114	...	75.4	-40.3	70.3	-43.2	79.2	-34.6	-0.126	0.043	0.208	0.036	0.0078	0.0027	-0.0082	0.0015	47.3	0.066	0.025
115	163	72.2	-29.4	68.4	-33.8	76.1	-26.5	0.007	0.008	-0.108	0.008	-0.0012	0.0007	0.0014	0.0013	80.84	-0.002	0.008
116	...	87.9	-36.4	85.5	-40.1	93.4	-33.3	0.321	0.059	-0.103	0.019	-0.0117	0.003	0.004	0.0008	52.67	0.082	0.029
117	...	94.0	-43.7	89.9	-46.2	100.6	-37.1	-0.06	0.083	0.362	0.078	0.0146	0.006	-0.0162	0.0035	47.49	0.068	0.017
118	80	106.9	-45.1	102.5	-54.9	114.5	-39.8	0.093	0.022	-0.065	0.032	-0.001	0.0023	-0.0049	0.0034	114.96	0.02	0.007
119	181	106.5	-37.0	104.0	-39.8	111.7	-34.0	0.277	0.025	0.058	0.018	-0.0053	0.0024	-0.0041	0.0008	80.57	-0.007	0.014
120	...	112.2	-38.3	108.4	-43.0	119.7	-34.3	0.091	0.021	0.023	0.012	0.0038	0.0026	-0.0027	0.0006	95.46	0.021	0.01
121	81	117.1	-43.4	114.5	-46.4	122.5	-39.0	0.305	0.06	0.091	0.013	-0.0131	0.0023	-0.0018	0.001	80.42	-0.047	0.012
122	193	120.3	-32.6	117.1	-35.7	124.8	-29.1	0.06	0.039	-0.006	0.013	-0.0031	0.0017	-0.0012	0.0012	85.13	0.001	0.005
123	187	113.6	-24.6	109.9	-28.9	117.9	-20.1	-0.007	0.016	-0.013	0.009	0.0025	0.0006	0.0	0.0006	65.47	-0.01	0.004
124	197	124.5	-23.9	122.0	-29.9	129.3	-22.0	0.10	0.017	-0.189	0.031	-0.0022	0.0019	0.0	0.0048	89.3	-0.007	0.002
125	195	121.8	-19.3	118.4	-22.6	124.7	-15.3	-0.025	0.011	-0.046	0.094	0.0019	0.0017	0.0123	0.0084	82.67	0.0	0.008
126	199	126.9	-20.7	124.6	-25.1	135.0	-18.2	0.102	0.029	-0.044	0.037	0.0075	0.004	-0.0058	0.0028	91.67	0.004	0.006
127	176	96.7	-19.4	92.5	-22.2	99.5	-15.9	-0.082	0.015	0.092	0.012	0.0004	0.0021	-0.0031	0.0014	35.28	0.067	0.016
128	83	-166.4	12.5	-173.2	7.5	-163.4	21.6	-0.151	0.022	0.115	0.056	-0.0058	0.0052	-0.0041	0.0136	21.83	0.02	0.012
129	84	-154.4	18.6	-161.8	13.7	-150.3	23.9	-0.262	0.108	0.109	0.053	0.0061	0.0065	-0.0052	0.0051	21.89	0.121	0.04
130	87	-145.4	30.0	-150.9	26.9	-142.1	35.4	-0.257	0.031	-0.053	0.045	0.0061	0.0019	0.0093	0.0023	31.94	-0.025	0.003
131	86	-150.6	36.6	-158.1	32.6	-147.6	41.4	-0.19	0.016	0.207	0.041	-0.0027	0.0034	-0.0103	0.0035	71.71	-0.03	0.003
132	88	-145.1	35.4	-152.0	32.8	-142.1	42.4	-0.038	0.05	0.067	0.035	-0.0115	0.0043	0.0089	0.004	40.83	-0.042	0.01
133	85	-152.0	41.6	-158.8	39.5	-149.8	47.3	-0.324	0.031	0.171	0.01	0.0075	0.004	0.0015	0.0027	33.15	0.10	0.046
134	220	-162.1	45.4	-171.3	41.2	-157.2	52.4	-0.223	0.027	0.224	0.03	-0.0016	0.0038	-0.0052	0.0023	62.13	-0.004	0.005
135	218	-183.1	53.5	-194.4	49.9	-178.7	59.9	-0.427	0.031	0.091	0.045	0.0005	0.0057	0.0068	0.004	19.94	0.039	0.019
136	219	-181.3	60.5	-191.3	55.5	-178.4	63.8	-0.146	0.131	-0.106	0.054	-0.0042	0.0057	0.0066	0.0029	12.89	0.14	0.043
137	222	-152.0	59.0	-160.4	53.3	-148.0	62.7	-0.19	0.028	-0.158	0.044	-0.0073	0.0047	0.0064	0.0032	25.12	0.008	0.015
138	94	-125.6	8.9	-132.5	1.2	-120.9	15.6	-0.05	0.018	0.019	0.006	-0.004	0.0019	0.0001	0.0007	54.89	0.014	0.01
139	101	-103.9	18.2	-110.1	14.6	-99.9	24.2	-0.099	0.058	0.099	0.024	0.0001	0.0039	-0.0001	0.0039	27.98	0.098	0.06
140	104	-94.3	6.3	-99.8	2.3	-90.9	11.4	-0.044	0.012	0.075	0.038	-0.0023	0.0025	-0.0023	0.0014	53.01	0.018	0.013

Table 2 continued on next page

Table 2 (continued)

knots	knot _{A95}	x	y	Box _{x1}	Box _{x2}	Box _{y1}	Box _{y2}	v_x	δv_x	v_y	δv_y	a_x	δa_x	a_y	δa_y	Peak Brightness	$\frac{\Delta F}{F}$	$\delta \frac{\Delta F}{F}$
(1)	(2)	(3)	(4)	(5)	(6)	(7)	(8)	(9)	(10)	(11)	(12)	(13)	(14)	(15)	(16)	(17)	(18)	(19)
141	105	-92.4	27.8	-97.8	22.8	-89.0	31.7	0.003	0.036	-0.109	0.057	-0.0085	0.0038	0.005	0.0041	38.56	-0.06	0.015
142	107	-89.7	15.0	-94.5	9.9	-86.0	20.0	-0.067	0.007	-0.044	0.015	0.0013	0.0007	0.003	0.0016	58.17	-0.021	0.006
143	110	-75.8	3.0	-83.5	-2.0	-71.2	9.0	-0.177	0.061	0.211	0.081	0.0004	0.0047	-0.0135	0.0031	40.08	-0.024	0.013
144	...	-63.6	25.8	-66.5	22.1	-57.6	28.8	0.172	0.028	-0.094	0.023	-0.0055	0.0014	0.0036	0.0012	38.8	0.011	0.011
145	112	-69.4	33.7	-74.1	30.5	-65.7	38.6	-0.002	0.041	0.035	0.017	-0.0052	0.0034	0.0031	0.0024	42.16	-0.02	0.016
146	114	-65.3	40.1	-71.9	36.8	-61.9	45.5	-0.222	0.023	0.038	0.012	0.006	0.002	0.0027	0.0013	48.12	0.031	0.012
147	116	-60.0	-7.4	-62.8	-12.6	-51.9	-2.9	0.425	0.073	0.124	0.047	-0.0172	0.0045	-0.0071	0.0035	44.57	-0.002	0.007
148	117	-48.8	-0.8	-52.9	-6.1	-43.5	3.7	-0.065	0.04	0.221	0.055	0.0035	0.003	-0.0158	0.0031	29.65	0.047	0.031
149	119	-36.9	6.8	-43.0	1.7	-33.6	10.2	-0.026	0.025	-0.051	0.028	-0.0033	0.0016	-0.0059	0.0026	33.38	0.011	0.015
150	120	-33.3	11.2	-37.4	6.3	-28.4	15.3	0.201	0.062	0.066	0.033	-0.0132	0.0134	-0.0057	0.0076	40.22	0.027	0.017
151	123	-17.6	10.5	-22.7	5.8	-12.7	15.9	-0.11	0.04	0.024	0.024	0.0063	0.003	0.004	0.0016	39.43	0.005	0.011
152	121	-24.8	38.2	-29.4	32.7	-17.9	42.9	0.066	0.02	-0.062	0.037	0.0046	0.004	0.0019	0.0055	46.57	-0.029	0.006
153	127	-0.9	17.9	-6.0	13.7	2.2	21.8	-0.022	0.039	0.001	0.012	-0.0029	0.004	0.0013	0.004	64.73	0.01	0.015
154	130	4.0	21.4	1.3	17.9	8.5	24.9	0.148	0.023	0.037	0.03	-0.0053	0.0022	-0.0015	0.0005	63.77	0.027	0.016
155	128	1.8	26.4	-1.2	22.4	5.4	30.2	0.098	0.016	0.022	0.014	-0.003	0.0006	-0.0014	0.0008	64.35	-0.033	0.009
156	...	15.2	26.1	12.6	22.1	17.9	28.7	0.038	0.016	-0.012	0.006	0.0014	0.0014	-0.0013	0.0005	48.88	-0.008	0.014
157	...	20.9	27.1	16.2	23.6	24.1	32.5	0.217	0.129	-0.045	0.124	-0.015	0.0116	0.0095	0.0124	50.9	0.03	0.012
158	137	18.2	34.7	14.1	31.7	22.3	40.7	0.168	0.05	0.124	0.108	-0.0084	0.0018	0.0004	0.0029	64.43	-0.025	0.018
159	262	22.1	43.0	19.0	40.0	27.0	49.9	0.047	0.029	0.088	0.027	-0.0002	0.0028	0.0023	0.0017	62.19	-0.028	0.008
160	144	31.3	-15.3	26.8	9.6	38.1	21.6	0.0	0.073	-0.11	0.085	0.0079	0.0056	0.0197	0.0067	53.29	0.068	0.024
161	145	33.2	30.7	29.4	24.5	38.3	33.9	0.04	0.034	-0.154	0.017	0.0002	0.0017	0.0022	0.0036	56.59	-0.018	0.002
162	147	35.2	36.9	32.4	32.9	39.7	41.2	0.171	0.015	0.002	0.022	-0.0038	0.0037	0.001	0.0022	53.29	-0.016	0.01
163	152	45.2	39.1	41.0	34.6	50.3	43.7	0.115	0.01	0.036	0.015	-0.0013	0.0012	0.0005	0.0011	75.42	0.033	0.01
164	...	45.1	31.8	41.6	27.2	52.8	36.8	0.303	0.047	-0.016	0.024	-0.0109	0.0021	0.0061	0.0029	60.79	0.10	0.033
165	155	52.3	22.9	49.0	19.6	60.8	26.4	0.229	0.011	0.083	0.02	-0.0015	0.0029	-0.0041	0.0011	66.52	-0.056	0.008
166	156	58.7	27.9	56.2	22.4	63.8	30.4	0.358	0.078	-0.276	0.06	-0.0166	0.0033	0.0119	0.0031	65.49	0.043	0.015
167	162	71.3	20.3	68.3	16.9	78.0	24.1	0.159	0.018	0.076	0.017	0.0015	0.0027	-0.0029	0.0015	65.49	-0.03	0.004
168	...	83.2	19.7	79.1	13.8	88.4	23.8	0.006	0.025	-0.085	0.014	0.0014	0.0018	0.0006	0.0015	46.06	0.013	0.007
169	169	84.9	26.5	81.0	20.4	89.5	29.3	-0.033	0.02	-0.165	0.025	0.0023	0.0019	0.003	0.0015	64.3	-0.035	0.009
170	171	89.9	32.3	85.3	28.0	96.6	37.4	0.095	0.014	0.071	0.014	-0.0002	0.0012	-0.0009	0.0012	56.22	0.018	0.011
171	172	90.5	-6.4	86.0	-9.8	93.4	-4.1	-0.131	0.045	-0.048	0.007	0.0072	0.0018	0.0001	0.0006	72.26	0.002	0.005
172	...	91.9	1.6	89.3	-1.7	97.4	4.6	0.233	0.088	0.122	0.057	-0.0142	0.004	-0.014	0.0033	50.74	0.045	0.019
173	174	95.2	-2.3	92.6	-5.4	99.9	1.5	0.185	0.024	0.09	0.019	-0.0054	0.0013	-0.004	0.0008	69.12	0.055	0.023
174	...	99.7	-9.9	95.4	-16.1	108.1	-6.1	0.123	0.155	-0.133	0.035	0.0021	0.0064	0.003	0.0027	83.24	0.007	0.011
175	186	113.4	-4.5	108.3	-9.0	117.6	0.2	-0.048	0.007	-0.015	0.012	0.0014	0.0005	0.0002	0.0002	122.64	0.026	0.02
176	183	107.8	6.8	104.8	2.6	113.2	9.8	0.227	0.023	-0.031	0.022	-0.0077	0.003	0.0011	0.0002	60.9	0.023	0.014

Table 2 continued on next page

Table 2 (continued)

knots	knot _{A95}	x	y	Box _{x,1}	Box _{x,2}	Box _{y,1}	Box _{y,2}	v_x	δv_x	v_y	δv_y	a_x	δa_x	a_y	δa_y	Peak Brightness	$\frac{\Delta B}{B}$	$\delta \frac{\Delta B}{B}$
(1)	(2)	(3)	(4)	(5)	(6)	(7)	(8)	(9)	(10)	(11)	(12)	(13)	(14)	(15)	(16)	(17)	(18)	(19)
177	180	106.2	14.6	100.5	10.4	109.9	18.4	-0.009	0.032	0.185	0.054	-0.0012	0.0049	-0.0097	0.0033	60.53	0.057	0.016
178	...	121.8	7.1	119.9	3.1	127.6	9.1	0.358	0.046	-0.057	0.011	-0.0121	0.0047	-0.0028	0.0016	68.34	0.041	0.011
179	...	122.0	-12	118.4	-16.2	127.7	-8.0	0.123	0.017	-0.061	0.028	-0.0004	0.0013	0.007	0.0017	94.81	0.051	0.016
180	202	131.3	-3.5	122.5	-10.5	134.9	0.6	-0.20	0.036	0.084	0.04	0.0002	0.0041	-0.0097	0.0023	187.92	-0.029	0.004
181	...	141.9	-6.2	139.1	-8.5	145.4	-2.8	0.133	0.023	0.093	0.025	-0.0044	0.0009	-0.0055	0.0011	87.55	0.023	0.015
182	209	143.6	-12.6	140.0	-16.6	150.9	-7.5	0.331	0.089	0.154	0.043	-0.0156	0.0056	-0.008	0.0023	127.25	0.0	0.004
183	210	146.3	-17.8	144.1	-21.1	151.2	-15.4	0.002	0.032	0.019	0.006	0.0067	0.0021	0.0001	0.0007	61.86	0.017	0.01
184	211	147.5	-7.6	144.5	-10.8	155.1	-3.9	0.265	0.023	0.062	0.02	-0.0009	0.004	-0.0038	0.0011	79.17	0.005	0.008
185	214	152.1	3.2	149.7	0.1	157.7	8.1	0.273	0.052	0.081	0.033	-0.0072	0.0025	-0.0011	0.0048	33.75	0.011	0.021
186	185	111.5	26.5	107.4	22.9	115.5	29.9	-0.176	0.04	-0.153	0.025	0.0096	0.0017	0.0056	0.001	66.95	0.046	0.023
187	190	117.3	33.7	113.3	30.4	119.7	35.7	-0.015	0.024	-0.07	0.014	-0.0041	0.0019	0.0028	0.0006	91.2	-0.036	0.012
188	194	120.7	25.5	114.7	22.4	123.9	31.1	-0.066	0.024	0.172	0.019	0.0001	0.0022	-0.0043	0.002	88.08	-0.016	0.002
189	201	130.1	19.8	127.6	15.8	137.3	25.1	0.257	0.104	-0.025	0.047	-0.0103	0.0045	0.0077	0.0029	47.94	0.031	0.019
190	207	139.4	19.4	135.3	13.1	147.6	24.2	0.325	0.025	-0.031	0.022	-0.0072	0.0042	0.0011	0.0002	37.12	0.10	0.04
191	208	143.5	26.9	141.1	22.7	152.6	31.7	0.351	0.025	-0.012	0.014	-0.0051	0.0038	0.0032	0.0019	17.87	0.036	0.019
192	...	118.2	40.7	114.6	32.3	125.1	44.7	0.197	0.03	-0.158	0.041	-0.0073	0.0015	-0.0082	0.0048	118.64	0.03	0.014
193	...	113.2	39.3	110.9	36.6	117.2	43.4	0.118	0.02	0.05	0.017	-0.0029	0.001	0.0027	0.0018	79.55	-0.014	0.003
194	287	127.0	42.5	124.6	38.8	134.9	47.3	0.193	0.007	0.083	0.02	0.0012	0.0029	-0.0041	0.0011	69.8	-0.011	0.013
195	286	111.3	47.6	108.3	42.1	117.7	51.8	0.146	0.018	0.038	0.017	-0.0044	0.0011	-0.0043	0.0011	69.82	-0.039	0.011
196	...	99.8	68.2	76.6	64.1	85.5	71.7	0.194	0.022	0.15	0.018	0.0001	0.0028	-0.004	0.0011	61.64	0.056	0.021
197	...	96.6	64.0	93.1	59.5	101.8	67.1	0.185	0.075	0.01	0.066	-0.0066	0.0081	-0.0049	0.0036	57.83	0.049	0.014
198	282	97.0	55.2	95.4	52.5	102.7	59.5	0.19	0.012	0.074	0.017	-0.0005	0.003	-0.0012	0.0016	86.77	0.033	0.015
199	280	94.1	48.7	91.0	45.8	100.8	52.7	0.311	0.041	-0.163	0.035	-0.0074	0.0022	0.0038	0.0027	107.45	0.045	0.019
200	...	82.4	46.0	80.0	42.2	89.1	51.1	0.274	0.072	0.019	0.025	-0.0127	0.0046	0.0058	0.0022	87.12	-0.048	0.007
201	278	76.2	46.3	72.0	42.3	81.9	50.3	0.121	0.017	0.025	0.008	-0.0025	0.0015	0.0014	0.0009	125.51	-0.023	0.005
202	276	67.7	42.6	63.9	39.3	73.4	47.9	0.012	0.018	0.044	0.006	0.0026	0.0011	0.0015	0.0011	114.81	0.009	0.007
203	216	-184.5	97.2	-195.3	94.5	-181.4	106.2	-0.258	0.024	0.127	0.042	-0.0047	0.0049	0.009	0.0059	12.57	0.183	0.049
204	221	-155.9	94.3	-167.8	90.4	-153.1	99.8	-0.318	0.074	0.191	0.035	-0.0057	0.0073	-0.004	0.0025	12.23	0.049	0.021
205	223	-150.1	97.1	-157.4	93.5	-146.4	102.5	-0.117	0.078	0.077	0.018	-0.0056	0.006	0.0003	0.0013	14.61	0.013	0.015
206	224	-142.3	117.2	-148.1	112.6	-138.8	121.6	-0.124	0.051	0.086	0.059	-0.0005	0.0029	-0.0026	0.0047	14.6	0.026	0.026
207	228	-122.5	106.2	-134.7	102.5	-118.4	113.5	-0.61	0.105	0.144	0.038	0.0149	0.0078	0.0047	0.0036	25.81	-0.031	0.013
208	...	-88.9	79.4	-95.9	75.3	-84.6	86.9	-0.095	0.052	0.048	0.036	0.0014	0.0009	0.0055	0.003	42.85	-0.048	0.004
209	232	-80.8	83.3	-88.3	78.6	-76.8	90.0	-0.047	0.024	0.228	0.058	-0.0056	0.0024	-0.012	0.0022	36.59	0.007	0.009
210	229	-91.7	65.1	-98.9	61.2	-87.0	71.7	-0.115	0.013	0.175	0.013	0.0026	0.0009	-0.0027	0.0017	64.24	0.002	0.008
211	230	-92.2	53.5	-97.6	48.7	-86.2	58.1	-0.083	0.039	0.058	0.018	-0.0003	0.0025	-0.0041	0.0008	56.46	0.011	0.018

Table 2 continued on next page

Table 2 (continued)

knots	knot _{A95}	x	y	Box _{x1}	Box _{x2}	Box _{y1}	Box _{y2}	v_x	δv_x	v_y	δv_y	a_x	δa_x	a_y	δa_y	Peak Brightness	$\frac{\Delta F}{F}$	$\delta \frac{\Delta F}{F}$
(1)	(2)	(3)	(4)	(5)	(6)	(7)	(8)	(9)	(10)	(11)	(12)	(13)	(14)	(15)	(16)	(17)	(18)	(19)
212	233	-76.9	58.4	-81.6	55.2	-71.6	64.1	0.112	0.029	0.223	0.012	-0.0056	0.0021	-0.0028	0.0022	65.05	-0.035	0.014
213	234	-73.3	65.7	-78.9	61.5	-67.0	72.4	0.092	0.039	0.162	0.011	-0.0033	0.0007	0.0002	0.0027	87.62	-0.03	0.003
214	235	-63.2	66.5	-71.5	62.6	-56.7	73.3	-0.061	0.014	0.106	0.016	0.0014	0.0011	-0.001	0.002	127.25	0.01	0.011
215	236	-60.6	58.9	-67.0	54.7	-57.1	63.8	-0.054	0.018	0.047	0.007	-0.0044	0.0021	-0.0001	0.0006	65.52	0.04	0.02
216	238	-50.4	68.1	-56.9	64.3	-45.7	75.2	-0.116	0.029	0.143	0.021	0.0051	0.0019	0.0028	0.003	77.26	-0.01	0.003
217	241	-37.0	64.2	-42.6	60.4	-34.7	67.8	-0.283	0.038	-0.078	0.032	0.0085	0.0019	0.0066	0.0013	49.45	0.062	0.018
218	240	-41.9	80.4	-46.2	75.2	-38.5	85.9	-0.06	0.028	-0.012	0.045	0.0025	0.0036	0.0062	0.0083	68.45	0.013	0.012
219	...	-42.2	86.4	-47.5	83.0	-37.5	93.0	0.083	0.029	-0.037	0.048	-0.004	0.001	0.016	0.0075	60.44	-0.052	0.008
220	239	-45.5	112.2	-53.3	107.7	-41.5	119.8	-0.026	0.056	-0.172	0.089	-0.0076	0.0034	0.0221	0.0062	35.18	-0.008	0.01
221	244	-32.1	110.2	-36.9	105.9	-27.0	115.7	0.099	0.01	0.051	0.007	-0.0011	0.0012	0.0003	0.0011	38.26	0.107	0.032
222	243	-34.1	83.4	-39.5	80.0	-28.0	90.6	0.057	0.021	0.188	0.007	-0.0028	0.001	-0.0014	0.0021	74.82	0.02	0.009
223	242	-34.8	73.9	-38.8	71.0	-30.6	79.2	-0.047	0.018	0.185	0.024	0.0046	0.0018	-0.0054	0.0013	64.66	-0.029	0.002
224	...	-28.4	71.8	-32.8	68.3	-23.0	77.7	0.109	0.038	0.043	0.01	-0.0048	0.0032	0.0016	0.0019	51.9	0.076	0.026
225	...	-21.1	92.0	-26.5	89.0	-18.1	100.3	-0.108	0.008	0.199	0.026	0.0014	0.0013	0.0011	0.0039	65.15	0.025	0.035
226	248	-17.2	86.8	-21.6	83.7	-11.3	93.9	0.018	0.028	0.105	0.02	0.0052	0.0017	0.0046	0.0031	83.62	0.004	0.01
227	246	-20.1	64.9	-25.2	61.1	-15.5	71.3	0.073	0.024	0.126	0.014	-0.0044	0.0009	0.0024	0.0025	54.17	0.065	0.027
228	245	-19.6	51.1	-25.7	48.1	-15.6	58.3	-0.033	0.033	0.154	0.017	-0.0035	0.0036	0.0022	0.0029	47.65	0.012	0.015
229	252	-4.1	66.1	-9.4	61.8	1.7	71.9	0.073	0.06	0.037	0.064	-0.0035	0.004	-0.001	0.0039	51.27	-0.042	0.009
230	255	-0.2	95.8	-3.0	93.4	2.8	103.2	0.016	0.006	0.119	0.037	-0.0015	0.0006	0.0062	0.0032	63.6	-0.041	0.007
231	256	3.1	82.1	-2.7	75.0	9.0	88.1	-0.012	0.008	-0.094	0.035	-0.0026	0.0014	0.0082	0.0026	79.83	-0.008	0.006
232	259	9.9	65.9	6.0	62.2	14.6	70.3	0.082	0.022	0.06	0.002	-0.0002	0.0013	-0.0001	0.0008	121.15	0.049	0.021
233	261	17.5	62.5	12.9	58.8	21.7	67.3	0.001	0.026	0.056	0.009	-0.0011	0.0024	-0.0004	0.001	101.87	-0.019	0.006
234	264	26.9	61.1	22.9	54.3	32.5	65.3	0.153	0.05	-0.16	0.023	-0.0107	0.0026	0.005	0.0037	91.98	-0.025	0.007
235	...	19.1	85.1	14.1	82.1	23.5	93.8	-0.038	0.025	0.32	0.014	0.0031	0.0028	-0.0033	0.0037	72.73	0.024	0.009
236	263	24.0	94.3	20.0	90.8	30.1	101.4	0.077	0.032	0.121	0.014	0.0018	0.0035	0.0031	0.0026	72.73	-0.007	0.008
237	265	26.9	86.2	23.6	83.0	31.9	92.5	0.038	0.017	0.105	0.006	-0.003	0.0007	0.0014	0.0018	100.41	0.01	0.004
238	267	28.8	99.7	25.9	94.5	34.7	103.9	0.201	0.026	-0.204	0.039	-0.0026	0.0025	0.0098	0.0018	71.13	0.106	0.042
239	271	39.0	87.2	33.8	81.7	43.2	90.9	-0.058	0.021	-0.113	0.048	-0.0002	0.0014	0.0078	0.0032	105.12	0.011	0.029
240	...	46.4	91.1	43.8	87.4	54.8	94.7	0.173	0.061	0.077	0.019	-0.0024	0.0053	-0.0013	0.002	79.64	-0.053	0.017
241	275	64.0	93.4	58.9	89.7	68.4	99.8	0.159	0.042	0.063	0.024	-0.01	0.0019	0.0027	0.0023	120.25	-0.005	0.008
242	...	80.0	68.8	96.7	65.5	107.4	73.8	0.06	0.049	-0.089	0.017	0.0008	0.0021	0.0053	0.0015	69.41	0.056	0.022
243	279	80.7	74.9	76.5	70.6	85.4	79.3	0.066	0.02	0.089	0.012	-0.0032	0.0007	-0.0016	0.0015	88.96	-0.006	0.003
244	...	81.8	98.9	76.0	94.2	87.6	104.9	0.09	0.019	0.13	0.019	-0.004	0.0008	-0.0016	0.0013	46.89	0.011	0.011
245	288	-9.5	139.4	-13.5	134.9	-4.2	146.3	0.006	0.035	0.129	0.056	0.0031	0.0016	-0.0051	0.0023	95.32	0.011	0.01
246	...	-5.6	153.4	-12.2	151.1	-2.9	163.0	-0.163	0.054	0.454	0.068	0.0051	0.0152	-0.0155	0.0072	27.49	0.123	0.043
247	291	1.5	173.0	-3.7	170.5	6.5	181.8	-0.051	0.012	0.305	0.015	0.0029	0.0006	0.0001	0.0042	41.51	0.055	0.015

Table 2 continued on next page

Table 2 (continued)

knots	knot _{A95}	x	y	Box _{x1}	Box _{x2}	Box _{y1}	Box _{y2}	v_x	δv_x	v_y	δv_y	a_x	δa_x	a_y	δa_y	Peak Brightness	$\frac{\Delta B}{B}$	$\delta \frac{\Delta B}{B}$
(1)	(2)	(3)	(4)	(5)	(6)	(7)	(8)	(9)	(10)	(11)	(12)	(13)	(14)	(15)	(16)	(17)	(18)	(19)
248	293	2.7	155.1	-1.6	152.7	10.1	165.7	0.058	0.055	0.469	0.022	-0.0007	0.0013	-0.0028	0.0128	14.39	0.153	0.045
249	294	8.8	135.9	3.8	131.8	13.1	142.0	0.092	0.012	0.032	0.009	-0.0031	0.0014	0.0015	0.0011	125.53	-0.005	0.007
250	...	11.7	150.3	9.1	148.4	17.0	158.7	0.135	0.033	0.42	0.063	-0.0051	0.0012	-0.0099	0.0036	15.33	-0.02	0.022
251	295	26.2	150.7	22.6	147.7	32.4	158.9	0.115	0.013	0.156	0.014	-0.0026	0.0009	0.003	0.0031	50.05	0.018	0.017
252	...	24.0	131.1	20.9	127.8	29.1	135.4	0.051	0.007	0.069	0.014	0.0003	0.0011	0.0009	0.0013	60.87	0.03	0.011
253	298	34.6	124.3	26.4	121.5	38.0	130.3	-0.383	0.054	0.133	0.006	0.0122	0.0028	0.0012	0.0021	75.25	0.015	0.007
254	...	41.7	147.0	36.0	144.8	45.6	153.7	-0.084	0.032	0.344	0.04	0.0054	0.0017	-0.0098	0.0025	12.57	0.087	0.026
255	...	40.3	126.4	37.2	123.2	45.3	133.0	-0.003	0.011	0.114	0.018	0.0029	0.001	0.0	0.0018	53.84	0.048	0.014
256	...	46.2	128.7	43.5	125.5	51.4	134.2	0.174	0.024	0.106	0.024	-0.0033	0.0013	0.0033	0.0026	55.54	-0.055	0.02
257	300	56.1	130.0	52.4	126.8	63.7	137.2	0.139	0.013	0.251	0.018	0.0013	0.0022	-0.0043	0.0025	71.23	0.035	0.015
258	302	63.8	148.7	60.7	145.9	70.1	157.0	0.114	0.018	0.295	0.033	0.0	0.0018	-0.0017	0.0048	17.21	0.016	0.015
259	303	72.9	134.6	70.1	132.1	79.5	142.6	0.13	0.013	0.236	0.028	-0.0029	0.001	0.002	0.0034	19.53	-0.003	0.009
260	304	79.9	136.4	77.1	133.8	90.9	145.5	0.703	0.107	0.512	0.076	-0.0229	0.0046	-0.014	0.0044	18.78	0.014	0.017

NOTE—Column 1: Number of each knot in this article; Column 2: Number of each knot same as in AR95; Column:3 and 4: Position of compact knots in the epoch 1987 continuum map, measured in arcsec and reference to the optical expansion center $\alpha(1950) = 23^{\text{h}}21^{\text{m}}11^{\text{s}}.4$, $\delta(1950) = +58^{\circ}32'28''.5$; Column 5 to 8: Box size defined for each knot, x_1, y_1, x_2, y_2 (arcsec), reference to the radio expansion center; Column 9: v_x , the proper motion of each knot in right ascension (arcsec yr⁻¹); Column 10: δv_x , uncertainty in right ascension proper motion; Column 11: v_y , the proper motion of each knot in declination (arcsec yr⁻¹); Column 12: δv_y , uncertainty in declination proper motion; Column 13: a_x , the acceleration of each knot in right ascension (arcsec yr⁻²); Column 14: δa_x , uncertainty in right ascension acceleration; Column 15: a_y , the acceleration of each knot in declination (arcsec yr⁻²); Column 16: δa_y , uncertainty in declination acceleration; Column 17: Peak brightness of each knot in 1987(mJy beam⁻¹); Column 18: $\frac{\Delta B}{B}$, annual percentage of the brightness change(percent yr⁻¹); Column 19: $\delta \frac{\Delta B}{B}$, uncertainty in fractional brightness change.

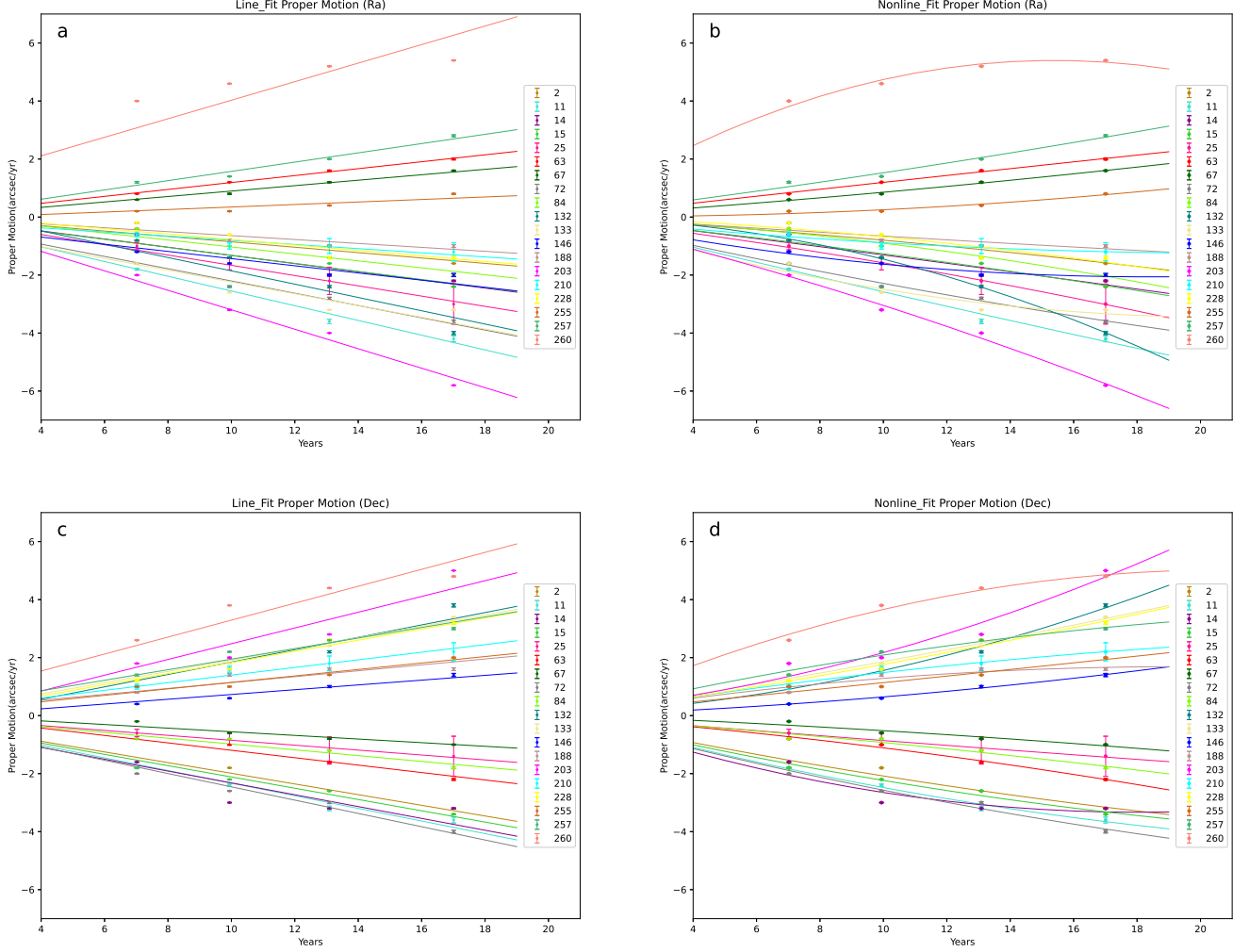


Figure 3. Fitting of linear and nonlinear models to partial knots' motion in Cas A. The figure "a" and "c" are the knots' proper motion fitted by linear model in Ra and Dec, respectively. The figure "b" and "d" are the knots' proper motion fitted by nonlinear model in Ra and Dec, respectively.

4. RESULTS AND DISCUSSION

The position (x, y) and peak brightness of all radio knot samples we studied are given in Table 2. The position respects to the optical expansion center of $\alpha(1950) = 23^{\text{h}}21^{\text{m}}11^{\text{s}}.4$, $\delta(1950) = +58^{\circ}32'28''.5$ (Koralesky et al. 1998). The quoted peak brightness is the maximum of the radio emission features. To determine the proper motion, acceleration or deceleration and brightness change ratio, nonlinear fitting method has been used. Proper motion (v_x, v_y) , acceleration or deceleration (a_x, a_y) , and brightness change ratio $(\frac{\Delta B}{B})$ fitting results are summarized in Table 2.

4.1. Proper Motions of Compact Radio Knots

We have used nonlinear fitting method to calculate the positional shifts $(\Delta\alpha$ and $\Delta\sigma)$ as a quadratic function of evolution time (i.e., $\Delta s = v_0 t + at^2$, Δs is the positional shifts of right ascension or declination), and obtained the proper motion of each radio features. The date of each VLA images adopted in the fitting is the average date of the A-, B-, C- and D-configuration observations of VLA. Most radio emissions in Cas A have decelerated significantly, nonlinear fitting can describe the real evolution of its motion better. From the linear and nonlinear model fits of partial knots' motion shown in Figure 3, linear fitting model does not provide a good fit to knots' motion trajectories, especially for knots with fast motion. The spatial distribution of proper motion vectors of the 260 radio knots is shown in Figure 4. Comparing with the plot of proper motion vectors in AR95, there is no significant systematic differences.

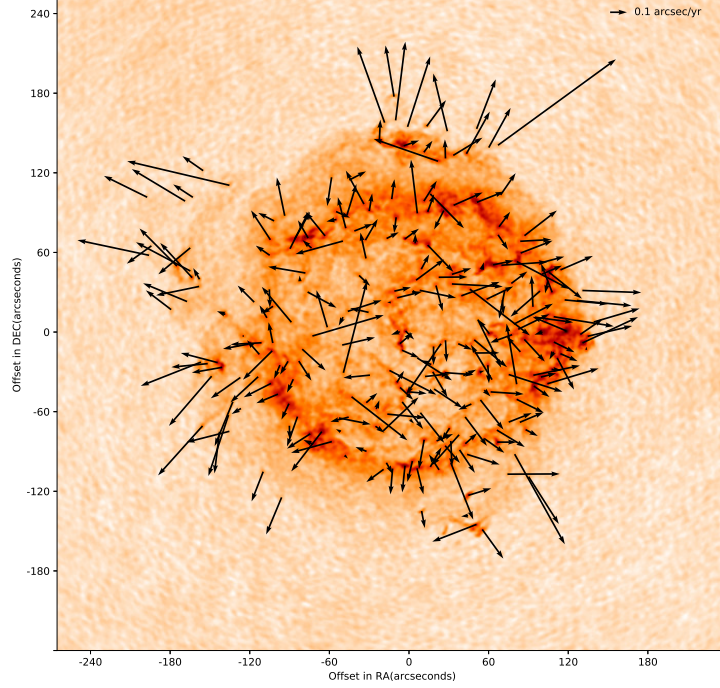


Figure 4. The spatial distribution of proper motion of 260 radio knots.

The location of radio expansion center is at $\alpha(1950) = 23^{\text{h}}21^{\text{m}}9^{\text{s}}.7 \pm 0^{\text{s}}.29$, $\delta(1950) = +58^{\circ}32'25''.2 \pm 2''.2$ from our measured proper motion results, which is consistent with the center position measured in AR95 within the quoted errors. A linear relationship between proper motion and distance from the radio expansion center has been used to deduce bulk expansion timescales of the remnant in AR95 and [Tuffs \(1986\)](#), which assumes that all radio emission have same initial velocity and does not show deceleration or experience the same deceleration process.

To track the motion evolution of Cas A, we used the same linear expansion model to estimate the expansion timescales of the remnant in right ascension and declination. Before fitting the relationship between proper motion and distance from the expansion center, we used the linear fitting method to recalculated the proper motion of

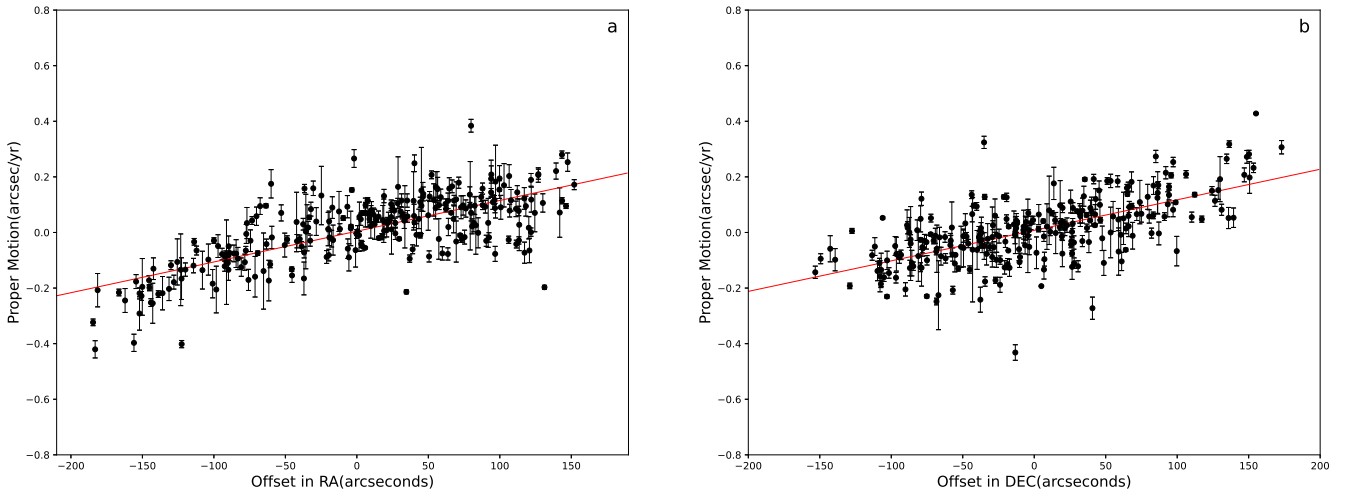


Figure 5. a: Linear weighted fits to the right ascension of proper motion as a function of radio knot position; b: Linear weighted fits to the declination of proper motion as a function of radio knot position

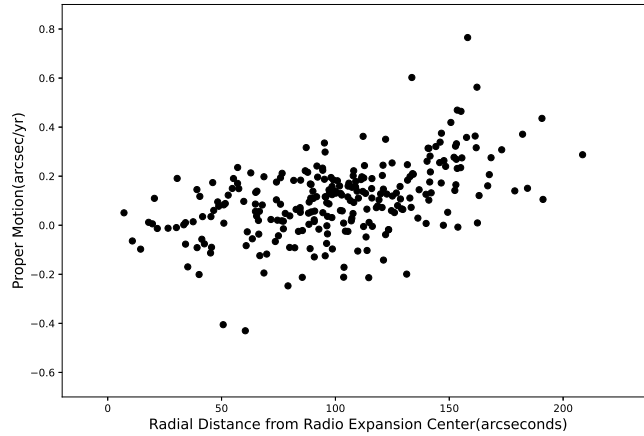


Figure 6. Projected radial proper motion vs. the distance from the radio expansion center.

radio features to ensure the rationality of this method. Figure 5 shows the fitting results of expansion timescales, the expansion timescales of right ascension is $T_{\text{RA}} = 904 \pm 10$ yrs, which equivalent to the expansion timescale of declination $T_{\text{DEC}} = 910 \pm 12$ yrs. Our measured expansion timescales is conflicts with Tuffs' (1986) measurement that the expansion timescales of right ascension was longer than declination significantly. Intriguingly, the expansion timescale in right ascension is approximates the expansion timescale in declination, which is consistent with AR95 ($T_{\text{RA}} = 866 \pm 8$ yrs, $T_{\text{DEC}} = 861 \pm 9$ yrs). However, the expansion timescales we obtained are longer. Under the assumption of a same expansion model we detected longer expansion timescales, which indicates that radio emission in the remnant were indeed deceleration.

The knots located at the northeastern and northern edges have relative high proper motion from the Figure 4, the velocity can reach to ~ 14500 km s^{-1} in the north. As shown in Figure 5a, the knots in located at the east and west under the fitting line are not well fitted, which indicates that knots have lower proper motion at the western and higher proper motion at the eastern. In the Figure 5b, the knots located at the northern are above the fitting line, indicating that the knots with higher proper motion in the north.

Ejecta interacting with the reverse shock forms a bright radio emission circle with a radius of ~ 1.7 pc in Cas A, and a fainter plateau extending to a radius of ~ 2.5 pc (Zirakashvili et al. 2014; DeLaney et al. 2014). This radio morphology corresponds to the two knots groups distributed in Figure 6, which can be understood as concentrically expanding shells as in AR95. Knots experience varying degrees of deceleration at different shells, and the proper motion of knots at the outer shell are faster than at the inner shell obviously. Moreover, the radial expansion ratio of radio emission features outside the bright radio ring increases with the distance from the radio expansion center. The average rate of expansion about 2100 km s^{-1} , while the nonlinearity values outer the bright radio ring is ~ 2550 km s^{-1} , and ~ 1750 km s^{-1} inner the bright radio ring. This expansion timescales in the bright ring region is ~ 857 yrs, and the outer region is ~ 525 yrs. The outer radio emission dynamic age of our measured close to the overall expansion timescales was measured by Agüeros & Green (1999) (i.e., ~ 400 -500 yrs). Interaction between the remnant and molecular clouds hints a deceleration of knots in the shell (Kilpatrick et al. 2014; Sato et al. 2018), outer shorter dynamics timescales indicate a smaller deceleration of knots located at the outer shell.

4.2. Accelerations of Compact Radio Knots

Longer expansion timescales have been detected using a same linear expansion model as for AR95, which indicates that the knots in Cas A have already decelerating significantly. In Section 4.1, the proper motion of 260 knots have been measured by using nonlinear fitting model ($\Delta s = v_0 t + a_s t^2$) to fit position shifts ($\Delta \alpha, \Delta \sigma$), meanwhile the magnitude of accelerations a_s has been given. For part knots, the computations of the position shifts appear in the opposite direction for some epochs, and the data of these epochs were excluded in fitting. For another, in order to calculate the accelerations of each knot, at least four epoch data are kept in the fitting (including the reference image). Therefore, part of the proper motions and the accelerations are calculated only based on data from four epochs. Those knots that position shifts in the opposite direction more than two epochs has been excluded in determining the used samples.

We have recalculated the accelerations of each knot by sequentially excluding each epoch from the fitting, the average significant level of a_{RA} and a_{DEC} around 2σ . For some knots, the obtained accelerations are less than the associated errors, which may be caused by the changes in shape or confusion with other emissions. Checking the spatial distribution of the accelerations, the accelerations field is somewhat disordered but not random noise. To determine individual knots are accelerating or decelerating directly, we project the accelerations onto the direction of its proper motion vectors. The spatial distribution of the acceleration vectors projection is displayed in Figure 7, which shows that $\sim 76\%$ of knots are decelerating. Taking as a whole, the components of the accelerations in the radial coordinates, right ascension and declination are $a_{\text{radial}} = -3.9 \pm 2.0 \text{ mas yr}^{-2}$, $a_{\text{RA}} = -1.7 \pm 0.7 \text{ mas yr}^{-2}$, $a_{\text{DEC}} = -2.6 \pm 1.0 \text{ mas yr}^{-2}$, respectively.

Vink et al. (2022) reported the proper motion of forward- and reverse-shock of Cas A in X-ray, and demonstrated that the forward shock in the western is accelerating. Most of the knots located at the outer edge of the northeast are shown accelerating from the measurement result displayed in Figure 7, but the spatial distribution of acceleration vectors in other regions appears to have no obvious regulations. The histogram peak flux in Figure 8 shows that there is no obvious difference between the acceleration and deceleration distribution, which hints that the acceleration or deceleration of individual knot have not correlation with the flux density distribution.

For the acceleration of radio emissions, we think there are two reasons. One is that the accelerated knots confuses with other radio emissions. Knots which locate in bright emission regions are more easily confuse with other radio emissions, and the acceleration is generally less than the quoted error. The second is that the stellar wind density of the remnant's progenitor is spatially inhomogeneous. Similarity in the morphology and spectra of the adjacent nebulae with the eastern cloud of Cas A indicates the progenitor's mass-loss (Weil et al. 2020). Mass-loss leads to the fluctuations in stellar wind density of progenitor, which will accelerate while a knot moves from high density region to low density region.

4.3. Brightness Changes of Compact Radio Knots

In the brightness change measurement, to avoid the influence of the difference of synthetic aperture coverage in difference epochs on the flux density and the shape of large-scale structures, we have smoothed all continuum images into a same beamsize (i.e., $1.5'' \times 1.5''$). Brightness changes have been measured using the least square method in Section 3.3, and the brightness change fraction was derived by nonlinear fitting. The spatial distribution of fractional changes in brightness is displayed in Figure 9. The flux of Cas A is constantly fading (Reichart & Stephens 2000;

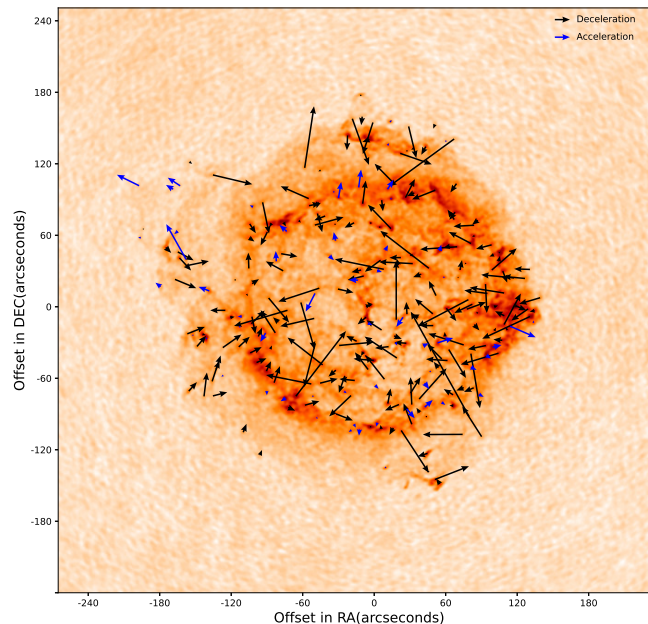


Figure 7. The spatial distribution of the acceleration vector projected in the proper motion vectors of the 260 radio knots. Black: the decelerated radio knots projected on the proper motion vector; Blue: the accelerated radio knots.

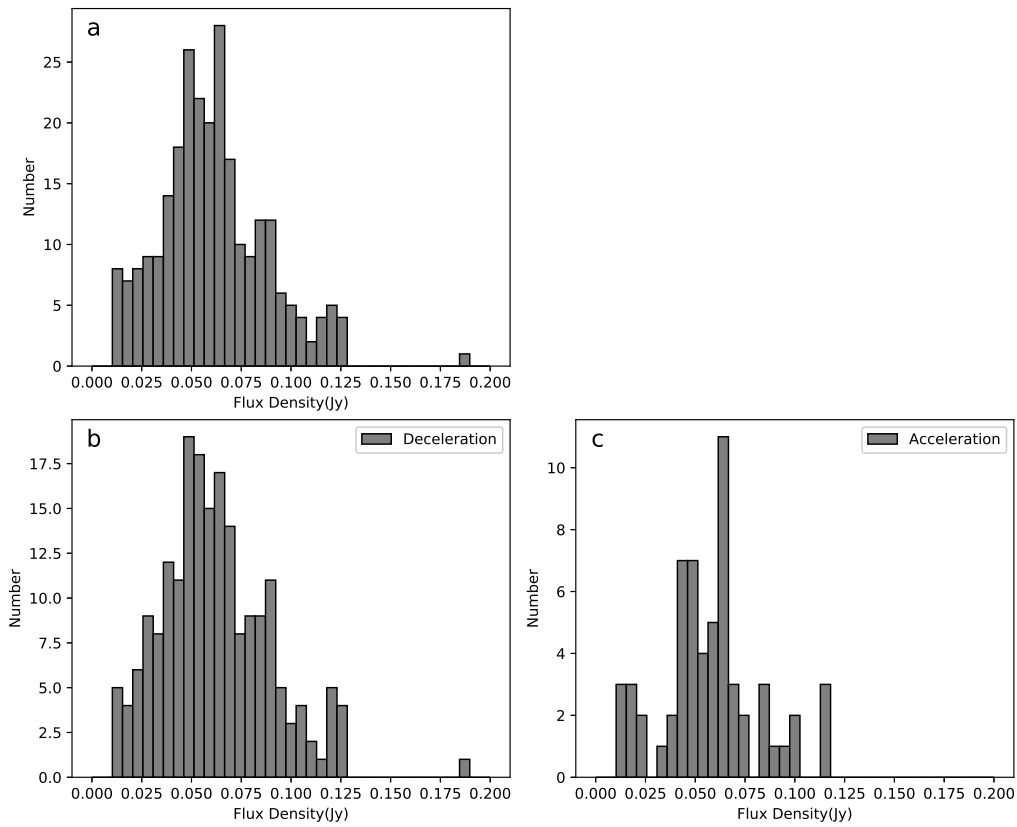


Figure 8. The histogram of peak flux of compact features we studied.

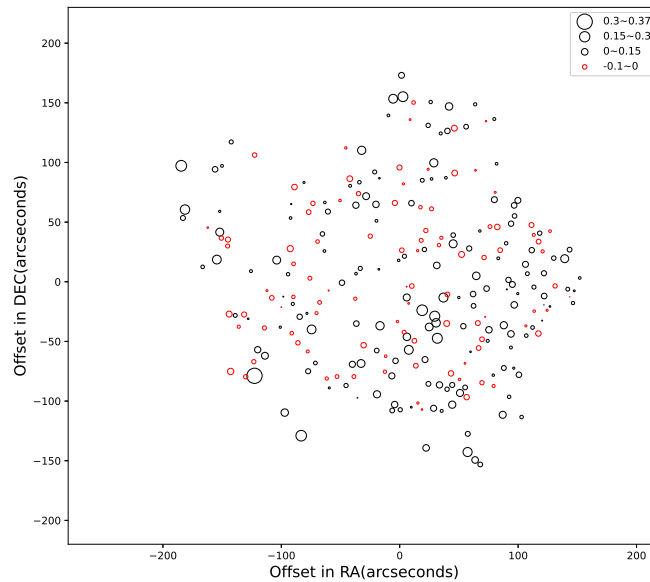


Figure 9. The fractional spatial distribution of brightness images of 260 compact radio knots.

Trotter et al. 2017). However, our measurement shows that $\sim 62\%$ of the radio knots are brightening with an average rate of $\sim 2.2\%$, these knots occupy only a small fraction of the total emission of Cas A.

AR95 has reported that the large-scale emission and compact features in Cas A are brightening with an average rate of $\sim 1.6\% \text{ yr}^{-1}$. In the current work, $\sim 62\%$ of the compact features are brightening, and the brightness changes fraction varies in different regions. The compact features on the bright radio ring ($90''\text{-}130''$) have a relatively low brightening rate of $\sim 1.4\% \text{ yr}^{-1}$. The average brightening rate of compact features in the inner of the bright radio ring ($\leq 90''$) is $\sim 2.1\% \text{ yr}^{-1}$, this value is mainly the contribution of the southwest region inside the bright radio ring, which is brightening rapidly. In the diffuse plateau region, compact features are brightening at a relatively fast rate of $3.7\% \text{ yr}^{-1}$.

Bright radio emissions rely on the synchrotron radiation emitted by electrons moving in magnetic field, a high radio emission means a high magnetic field for a given number density of electrons. Most of the radio-bright knots are distributed in the bright ring of Cas A from Figure 2, whereas the primary site of cosmic-ray acceleration located in the forward shock front (Vink & Laming 2003; Helder et al. 2012). Moreover, studies of radio spectral index have shown no evidence of reacceleration in bright radio knots (Anderson & Rudnick 1996; Wright et al. 1999). These studies indicate that brightness variations are links to the fluctuations of magnetic field directly. Therefore, the fading, brightening, disappearing or new appearing of compact features in Cas A are likely to be the result of magnetic field variations.

5. SUMMARY

We have obtained five images of Cas A at 5 GHz in all four configurations of the VLA from 1987 to 2004, while all images have been smoothed to the same resolution of $1.5''$. We measured the proper motion and brightness changes of compact radio features in Cas A, gave the radio expansion center locates at $\alpha(1950) = 23^{\text{h}}21^{\text{m}}9^{\text{s}}7 \pm 0^{\text{s}}29$, $\delta(1950) = +58^{\circ}32'25''2 \pm 2''$, and the expansion timescales of right ascension and declination: $T_{\text{RA}} = 904 \pm 10$ yrs, $T_{\text{DEC}} = 910 \pm 12$ yrs, respectively. Because of the limit of angular resolution of observation, the uncertainty of proper motion measurement will lead to different estimation for the expansion timescale. Benefiting from the improvement in angular resolution, the expansion timescale is more reliable.

The remnant is overall in a decelerating phase, but only about three-quarters of compact radio knots are decelerating. Some radio knots with acceleration are in the region of radio emission confusion and these radio knots may not really be in acceleration. In addition to the effect of measurement errors in the radio emission confusion regions, the compact features' acceleration phenomenon suggests that there is density fluctuation in the stellar wind of Cas A's progenitor. During 17 yrs, the brightness of the compact radio features in Cas A has changed significantly, which suggests that the magnetic field is changing rapidly.

We thank Dr. Shi Hui and Dr. Yang Ai-Yuan for the guidance on data calibration in this work. We acknowledge support from the National Key R&D Programs of China (2018YFA0404203, 2018YFA0404202), National Natural Science Foundation of China (12041301, 12073039) and the China Manned Space Project (CMS-CSST-2021-A09). We thank the staff of the Karl G. Jansky Very Large Array for the observation of Cassiopeia A.

REFERENCES

- Agüeros, M. A., & Green, D. A. 1999, MNRAS, 305, 957, doi: [10.1046/j.1365-8711.1999.02504.x](https://doi.org/10.1046/j.1365-8711.1999.02504.x)
- Ahnen, M. L., Ansoldi, S., Antonelli, L. A., et al. 2017, MNRAS, 472, 2956, doi: [10.1093/mnras/stx2079](https://doi.org/10.1093/mnras/stx2079)
- Allen, G. E., Keohane, J. W., Gotthelf, E. V., et al. 1997, ApJL, 487, L97, doi: [10.1086/310878](https://doi.org/10.1086/310878)
- Anderson, M. C., & Rudnick, L. 1995, ApJ, 441, 307, doi: [10.1086/175357](https://doi.org/10.1086/175357)
- . 1996, ApJ, 456, 234, doi: [10.1086/176644](https://doi.org/10.1086/176644)
- Ashworth, W. B., J. 1980, Journal for the History of Astronomy, 11, 1, doi: [10.1177/002182868001100102](https://doi.org/10.1177/002182868001100102)
- Bell, A. R. 1977, MNRAS, 179, 573, doi: [10.1093/mnras/179.4.573](https://doi.org/10.1093/mnras/179.4.573)
- Bell, A. R., Gull, S. F., & Kenderdine, S. 1975, Nature, 257, 463, doi: [10.1038/257463a0](https://doi.org/10.1038/257463a0)
- Chevalier, R. A., & Kirshner, R. P. 1978, ApJ, 219, 931, doi: [10.1086/155855](https://doi.org/10.1086/155855)
- . 1979, ApJ, 233, 154, doi: [10.1086/157377](https://doi.org/10.1086/157377)
- Cornwell, T. J. 2008, IEEE Journal of Selected Topics in Signal Processing, 2, 793, doi: [10.1109/JSTSP.2008.2006388](https://doi.org/10.1109/JSTSP.2008.2006388)
- DeLaney, T., Kassim, N. E., Rudnick, L., & Perley, R. A. 2014, ApJ, 785, 7, doi: [10.1088/0004-637X/785/1/7](https://doi.org/10.1088/0004-637X/785/1/7)
- DeLaney, T., & Rudnick, L. 2003, ApJ, 589, 818, doi: [10.1086/374813](https://doi.org/10.1086/374813)

- DeLaney, T., Rudnick, L., Fesen, R. A., et al. 2004, *ApJ*, 613, 343, doi: [10.1086/422906](https://doi.org/10.1086/422906)
- Dickel, J. R., & Greisen, E. W. 1979, *A&A*, 75, 44
- Fesen, R. A. 2001, *ApJS*, 133, 161, doi: [10.1086/319181](https://doi.org/10.1086/319181)
- Fesen, R. A., Becker, R. H., & Blair, W. P. 1987, *ApJ*, 313, 378, doi: [10.1086/164974](https://doi.org/10.1086/164974)
- Fesen, R. A., Becker, R. H., & Goodrich, R. W. 1988, *ApJL*, 329, L89, doi: [10.1086/185183](https://doi.org/10.1086/185183)
- Fesen, R. A., Morse, J. A., Chevalier, R. A., et al. 2001, *AJ*, 122, 2644, doi: [10.1086/323539](https://doi.org/10.1086/323539)
- Fesen, R. A., Hammell, M. C., Morse, J., et al. 2006, *ApJ*, 645, 283, doi: [10.1086/504254](https://doi.org/10.1086/504254)
- Gotthelf, E. V., Koralesky, B., Rudnick, L., et al. 2001, *ApJL*, 552, L39, doi: [10.1086/320250](https://doi.org/10.1086/320250)
- Grefenstette, B. W., Reynolds, S. P., Harrison, F. A., et al. 2015, *ApJ*, 802, 15, doi: [10.1088/0004-637X/802/1/15](https://doi.org/10.1088/0004-637X/802/1/15)
- Helder, E. A., & Vink, J. 2008, *ApJ*, 686, 1094, doi: [10.1086/591242](https://doi.org/10.1086/591242)
- Helder, E. A., Vink, J., Bykov, A. M., et al. 2012, *SSRv*, 173, 369, doi: [10.1007/s11214-012-9919-8](https://doi.org/10.1007/s11214-012-9919-8)
- Hogg, D. E., MacDonald, G. H., Conway, R. G., & Wade, C. M. 1969, *AJ*, 74, 1206, doi: [10.1086/110924](https://doi.org/10.1086/110924)
- Hughes, J. P., Rakowski, C. E., Burrows, D. N., & Slane, P. O. 2000, *ApJL*, 528, L109, doi: [10.1086/312438](https://doi.org/10.1086/312438)
- Hwang, U., & Laming, J. M. 2012, *ApJ*, 746, 130, doi: [10.1088/0004-637X/746/2/130](https://doi.org/10.1088/0004-637X/746/2/130)
- Inoue, T., Yamazaki, R., Inutsuka, S.-i., & Fukui, Y. 2012, *ApJ*, 744, 71, doi: [10.1088/0004-637X/744/1/71](https://doi.org/10.1088/0004-637X/744/1/71)
- Kilpatrick, C. D., Biegging, J. H., & Rieke, G. H. 2014, *ApJ*, 796, 144, doi: [10.1088/0004-637X/796/2/144](https://doi.org/10.1088/0004-637X/796/2/144)
- Koralesky, B., Rudnick, L., Gotthelf, E. V., & Keohane, J. W. 1998, *ApJL*, 505, L27, doi: [10.1086/311604](https://doi.org/10.1086/311604)
- Krause, O., Birkmann, S. M., Usuda, T., et al. 2008, *Science*, 320, 1195, doi: [10.1126/science.1155788](https://doi.org/10.1126/science.1155788)
- Maeda, Y., Uchiyama, Y., Bamba, A., et al. 2009, *PASJ*, 61, 1217, doi: [10.1093/pasj/61.6.1217](https://doi.org/10.1093/pasj/61.6.1217)
- McMullin, J. P., Waters, B., Schiebel, D., Young, W., & Golap, K. 2007, in *Astronomical Society of the Pacific Conference Series*, Vol. 376, *Astronomical Data Analysis Software and Systems XVI*, ed. R. A. Shaw, F. Hill, & D. J. Bell, 127
- Morse, J. A., Fesen, R. A., Chevalier, R. A., et al. 2004, *ApJ*, 614, 727, doi: [10.1086/423709](https://doi.org/10.1086/423709)
- Orlando, S., Wongwathanarat, A., Janka, H. T., et al. 2022, *A&A*, 666, A2, doi: [10.1051/0004-6361/202243258](https://doi.org/10.1051/0004-6361/202243258)
- Patnaude, D. J., & Fesen, R. A. 2007, *AJ*, 133, 147, doi: [10.1086/509571](https://doi.org/10.1086/509571)
- . 2009, *ApJ*, 697, 535, doi: [10.1088/0004-637X/697/1/535](https://doi.org/10.1088/0004-637X/697/1/535)
- . 2014, *ApJ*, 789, 138, doi: [10.1088/0004-637X/789/2/138](https://doi.org/10.1088/0004-637X/789/2/138)
- Perley, R. A., & Butler, B. J. 2013, *ApJS*, 204, 19, doi: [10.1088/0067-0049/204/2/19](https://doi.org/10.1088/0067-0049/204/2/19)
- Reed, J. E., Hester, J. J., Fabian, A. C., & Winkler, P. F. 1995, *ApJ*, 440, 706, doi: [10.1086/175308](https://doi.org/10.1086/175308)
- Reichart, D. E., & Stephens, A. W. 2000, *ApJ*, 537, 904, doi: [10.1086/309073](https://doi.org/10.1086/309073)
- Rosenberg, I. 1970, *MNRAS*, 151, 109, doi: [10.1093/mnras/151.1.109](https://doi.org/10.1093/mnras/151.1.109)
- Sano, H., & Fukui, Y. 2021, *Ap&SS*, 366, 58, doi: [10.1007/s10509-021-03960-4](https://doi.org/10.1007/s10509-021-03960-4)
- Sato, T., Katsuda, S., Morii, M., et al. 2018, *ApJ*, 853, 46, doi: [10.3847/1538-4357/aaa021](https://doi.org/10.3847/1538-4357/aaa021)
- Thorstensen, J. R., Fesen, R. A., & van den Bergh, S. 2001, *AJ*, 122, 297, doi: [10.1086/321138](https://doi.org/10.1086/321138)
- Trotter, A. S., Reichart, D. E., Egger, R. E., et al. 2017, *MNRAS*, 469, 1299, doi: [10.1093/mnras/stx810](https://doi.org/10.1093/mnras/stx810)
- Tuffs, R. J. 1986, *MNRAS*, 219, 13, doi: [10.1093/mnras/219.1.13](https://doi.org/10.1093/mnras/219.1.13)
- Uchiyama, Y., & Aharonian, F. A. 2008, *ApJL*, 677, L105, doi: [10.1086/588190](https://doi.org/10.1086/588190)
- Vink, J., & Laming, J. M. 2003, *ApJ*, 584, 758, doi: [10.1086/345832](https://doi.org/10.1086/345832)
- Vink, J., Patnaude, D. J., & Castro, D. 2022, *ApJ*, 929, 57, doi: [10.3847/1538-4357/ac590f](https://doi.org/10.3847/1538-4357/ac590f)
- Weil, K. E., Fesen, R. A., Patnaude, D. J., et al. 2020, *ApJ*, 891, 116, doi: [10.3847/1538-4357/ab76bf](https://doi.org/10.3847/1538-4357/ab76bf)
- Willingale, R., Bleeker, J. A. M., van der Heyden, K. J., Kaastra, J. S., & Vink, J. 2002, *A&A*, 381, 1039, doi: [10.1051/0004-6361:20011614](https://doi.org/10.1051/0004-6361:20011614)
- Wright, M., Dickel, J., Koralesky, B., & Rudnick, L. 1999, *ApJ*, 518, 284, doi: [10.1086/307270](https://doi.org/10.1086/307270)
- Zirakashvili, V. N., Aharonian, F. A., Yang, R., Oña-Wilhelmi, E., & Tuffs, R. J. 2014, *ApJ*, 785, 130, doi: [10.1088/0004-637X/785/2/130](https://doi.org/10.1088/0004-637X/785/2/130)